ACS Catalysis

Research Article

pubs.acs.org/acscatalysis

Ab Initio-Based Kinetic Modeling for the Design of Molecular Catalysts: The Case of H_2 Production Electrocatalysts

Ming-Hsun Ho, Roger Rousseau, John A. S. Roberts, Eric S. Wiedner, Michel Dupuis, Daniel L. DuBois, R. Morris Bullock, and Simone Raugei*

Center for Molecular Electrocatalysis, Pacific Northwest National Laboratory, P.O. Box 999, K1-83, Richland, Washington 99352, United States

Supporting Information

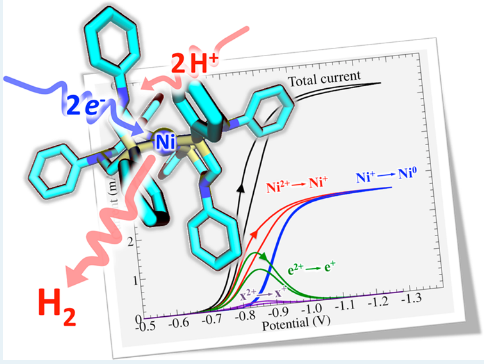

ABSTRACT: Design of fast, efficient electrocatalysts for energy production and energy utilization requires a systematic approach to predict and tune the energetics of reaction intermediates and the kinetic barriers between them as well as to tune reaction conditions (e.g., concentration of reactants, acidity of the reaction medium, and applied electric potential). Thermodynamics schemes based on the knowledge of pK_a values, hydride donor ability, redox potentials, and other relevant thermodynamic properties have been demonstrated to be very effective for exploring possible reaction pathways. We seek to identify high-energy intermediates, which may represent a catalytic bottleneck, and low-energy intermediates, which may represent a thermodynamic sink. In this study, working on a well-established Ni-based bioinspired electrocatalyst for H_2 production, we performed a detailed kinetic analysis of the catalytic pathways to assess the limitations of our current (standard state) thermodynamic analysis with respect to prediction of optimal catalyst performance. To this end, we developed a microkinetic model based on extensive ab initio simulations. The model was validated against available experimental data, and it reproduces remarkably well the observed turnover rate as a function of the acid concentration and catalytic conditions, providing valuable information on the main factors limiting catalysis. Using this kinetic analysis as a reference, we show that indeed a purely thermodynamic analysis of the possible reaction pathways provides us with valuable information, such as a qualitative picture of the species involved during catalysis, identification of the possible branching points, and the origin of the observed overpotential, which are critical insights for electrocatalyst design. However, a significant limitation of this approach is understanding how these insights relate to rate, which is an equally critical piece of information. Taking our analysis a step further, we show that the kinetic model can easily be extended to different catalytic conditions by using linear free energy relationships for activation barriers based on simple thermodynamics quantities, such as pK_a values. We also outline a possible procedure to extend it to other catalytic platforms, making it a general and effective way to design catalysts with improved performance.

KEYWORDS: *electrocatalysis, H_2 production, ab initio calculations, molecular dynamics, free energy simulations, microkinetic modeling*

INTRODUCTION

Rapid design of the next generation of catalysts for energy applications requires a systematic method to tune the energetics of reaction intermediates and the kinetic barriers between them. By recognizing that many reactions, such as H_2 production and oxidation and O_2, N_2, and CO_2 reduction, involve electrons, protons, and hydride transfers, our group has proposed a thermodynamic approach[1−6] to avoid high- and low-energy intermediates, which may introduce high activation barriers and thermodynamics sinks. This approach is based on the realization that an efficient catalytic transformation requires the flattest free energy profile possible, with small free energy changes between consecutive steps.[1] This approach has revealed itself to be very powerful, providing design criteria for molecular catalysts for renewable energy utilization systems.[5,7] However, catalysis is by definition a kinetic phenomenon in which both rates (activity) and selectivity can be varied by changes in the reaction conditions (temperature and pressure), concentration of the various species, acidity of the medium, etc. Thus, design of an ideal catalyst cannot be achieved solely through thermodynamic considerations; chemical kinetics under operating conditions must also be taken into account.

The fundamental question examined in this paper is a consideration of the limits of our current standard state thermodynamic analysis with respect to predicting optimal catalyst performance and determining the additional insights that can be garnered from a kinetics perspective. A major objective of this study is to probe and quantify the limitations of a purely thermodynamics-based paradigm for designing

Received: June 3, 2015
Revised: July 21, 2015
Published: July 30, 2015

DOI: 10.1021/acscatal.5b01152
ACS Catal. 2015, 5, 5436−5452

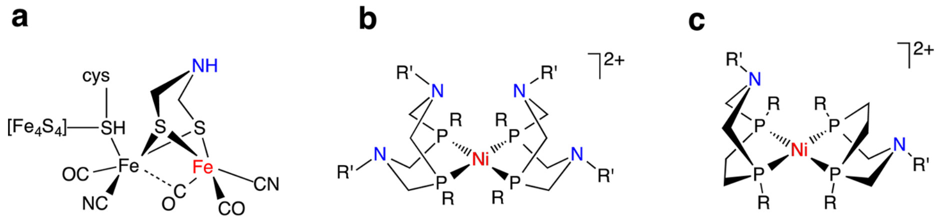

Figure 1. Active site of the [FeFe] hydrogenase enzyme (a) and synthetic catalysts for H_2 oxidation and production: (b) $[\mathrm{Ni}(\mathrm{P}^{\mathrm{R}}_2\mathrm{N}^{\mathrm{R}'}_2)_2]^{2+}$ with $\mathrm{P}^{\mathrm{R}}_2\mathrm{N}^{\mathrm{R}'}_2$ = 1,5-R′-3,7-R-1,5-diaza-3,7-diphosphacyclooctane; (c) $[\mathrm{Ni}(7\mathrm{P}^{\mathrm{R}}_2\mathrm{N}^{\mathrm{R}'})_2]^{2+}$ with $7\mathrm{P}^{\mathrm{R}}_2\mathrm{N}^{\mathrm{R}'}$ = 1-R′-3,6-R-1-aza-3,6-diphosphacycloheptane.

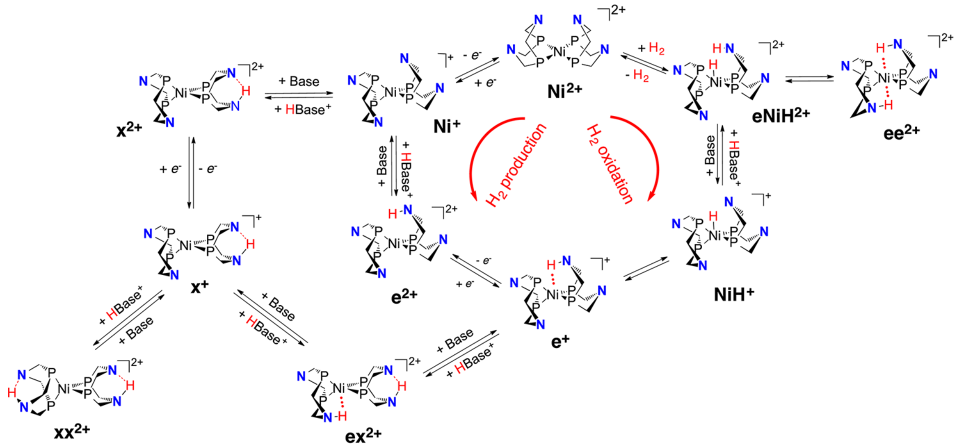

Figure 2. Proposed mechanism for H_2 oxidation (clockwise) and H_2 formation (counterclockwise) catalyzed by $[\mathrm{Ni}(\mathrm{P}^{\mathrm{R}}_2\mathrm{N}^{\mathrm{R}'}_2)_2]^{2+}$ complexes in the presence of an exogenous base (base) or acid (Hbase$^+$). For clarity, the substituents R and R′ are not shown.

molecular catalysts. Catalysis is performed under a kinetic steady state, not at thermodynamic equilibrium, yet details of concentrations of species at steady state depend on the underpinning free energy landscape, which is not available a priori. Recognizing this intrinsic limitation, we ask the fundamental question about the limitations of a standard state thermodynamic analysis for catalyst design.

Utilization of microkinetic modeling, wherein each elementary chemical step is accounted for and the reaction kinetics are followed in time by numerically solving the coupled differential equations defining the reaction network, is ubiquitous in heterogeneous catalysis.[8−14] These simulations reveal how reactivity varies with thermodynamic conditions, which are included as input parameters and reactor configurations given in terms of boundary conditions. Despite their utility, often necessity, in modeling heterogeneous processes, microkinetic models are far less common in studies of homogeneous catalysts. This paucity of studies for homogeneous catalysts is perplexing considering that the well-defined nature of homogeneous catalysts lends itself more readily to detailed quantitation of individual reaction events from either experiment or modeling than it does for heterogeneous counterparts. In heterogeneous systems, the nature of catalytic intermediates and even of the catalytic centers remain often elusive. In contrast, molecular catalysts offer an ideal platform to build a much more comprehensive computational representation because reaction energy barriers can be determined with high accuracy.[15,16] In this paper, we greatly increase our understanding of molecular electrocatalysts for evolution of H_2, and we develop a reliable microkinetic model from detailed ab initio data. We use this kinetic model in conjunction with our thermodynamic analysis to infer general principles that allow us to control catalytic pathways, promoting efficient routes over the multitude of possible catalytic pathways.

To achieve this goal, we focus on an extensively well-documented and quantified Ni-based molecular catalyst,[17−22] which we have studied in the context of the proton reduction reaction. We first demonstrate that our microkinetic model reproduces both overall trends in reactivity as a function of voltage and species concentration, and we rationalize many subtle details of the chemical conversions that have been observed but hitherto not well understood. This allows us to validate our microkinetic model and provides evidence that the quantitative measure of the kinetic steady state is meaningful.

More specifically, we have been studying electrocatalytic processes based on inexpensive, earth-abundant metals[23] that rapidly and efficiently interconvert electrical energy and fuels for renewable energy utilization systems.[24−29] Most of the reactions involved in electrochemical transformations require movement of protons within the catalyst and between the catalyst and an external acid or base. Recent studies have highlighted the importance of proton movement for efficient catalytic conversions.[7,30,31] From this large data set of experiments and computations, we have developed and validated quantitative descriptions of both the reaction energy and the barrier for many of the individual chemical steps in the catalytic cycle for electrochemical H_2 production and oxidation by Ni-based electrocatalysts, thereby allowing us to construct a microkinetic model with an unprecedented level of accuracy. Specifically, detailed experimental and computational investigations revealed the necessity of facile and controlled (in space and time) proton delivery to achieve fast catalytic rates at low overpotentials.[32−34]

The catalyst discussed in this paper, $[Ni(P^{Ph}_2N^{Ph}_2)_2]^{2+}$, is part of a family of electrocatalysts for H_2 oxidation and production inspired by [FeFe] hydrogenase. These enzymes oxidize and produce H_2 at high rates (turnover frequency, TOF > 10 000 s^{-1}) and at low overpotentials (~100 mV).[35,36] The presence of a noncoordinating pendant amine in the second coordination sphere of a catalytic Fe center (Figure 1a), incorporated in a six-membered ring, has been shown to facilitate H_2 bond cleavage and formation. The introduction of an amine functionality in the diphosphine ligand in molecular electrocatalysts leads to improved rates and overpotentials.[7] The majority of our studies focused on diphosphine ligands with one or two amines (Figure 1b,c).[17,20,37−43] The catalytic bias (H_2 oxidation or H_2 production)[44,45] and efficiency (overpotential) of the catalysts can be tuned by changing the substituents R and R′. These synthetic Ni catalysts can produce H_2 at TOF > 10^7 s^{-1}[46] and oxidize H_2 at TOF > 200 s^{-1}.[39,47,48] With only a few exceptions,[47,49] overpotentials for catalysts operating at these high rates remain large (>200 mV).[7]

The proposed mechanism of catalysis involves a sequence of intramolecular proton movements, intermolecular deprotonation and protonation steps, and electrochemical events. The proposed catalytic mechanism for $[Ni(P^{R}_2N^{R'}_2)_2]^{2+}$ catalysts (Figure 1b) is reported in Figure 2. NMR spectroscopy[33,34] and electrochemical investigations,[32] combined with theoretical calculations,[19,33,34,38,50] have been employed to study proton movement in these catalysts, highlighting its role for efficient catalytic processes. For H_2 oxidation catalysis (Figure 2, clockwise direction), previous studies showed that addition of H_2 results in the heterolytic splitting of the molecule and the subsequent formation of a Ni(0) doubly endo N-protonated intermediate, **ee**$^{2+}$, via a N-protonated Ni(II) hydride species.[19,51,52] In this paper, protonation of the pendant amine endo to the metal center is denoted with **e**, protonation of the pendant amine exo to the metal center is denoted with **x**, protonation at the metal center to make the nickel hydride is denoted with **NiH** (see Figure S1). Overall charges are as indicated. The **ee**$^{2+}$ doubly protonated intermediate is characterized by two N−H groups pointing toward the metal center (endo with respect to metal center). Isomerization of this species, involving intermolecular deprotonation and protonation events, leads to the stepwise formation of exo protonated species, in which the proton is pointing away from the metal center (species **ex**$^{2+}$ and **xx**$^{2+}$).[33,38,53] In the case of $P^{R}_2N^{R'}_2$ ligands, the exo protons can be stabilized via intramolecular hydrogen bonding, giving rise to "pinched" structures, such as those shown in Figure 2,[19] which have been proposed to slow the catalytic rate.[33,38] Kinetic and computational studies showed that in nonaqueous solvents, the rate of isomerization is limited by proton removal from, or delivery to, the complex.[33] The H_2 oxidation cycle is closed by an electrochemical oxidation and deprotonation steps (via an exogenous base).

Hydrogen production has been generally proposed to follow an initial electrochemical reduction of the Ni(II) complex, followed by protonation of the catalyst in an electron−proton−electron−proton (ECEC) sequence (Figure 2, counterclockwise direction). Different sequences of electrochemical and thermochemical steps can also be envisioned, depending on the applied potential and the strength of the exogenous acid. In addition, the presence of multiple protonation sites adds a further degree of complexity with the formation of a variety of endo- or exoprotonated isomers. Here, we seek an understanding of how the presence of different isomers connected by different catalytic pathways influences the rate of production of H_2. Then we show how this information can be used to control which intermediates should be formed and, therefore, how to control catalytic rates.

■ RESULTS AND DISCUSSION

The electrocatalytic process for H_2 production and oxidation is shown in eq 1.

$$2BH^+ + 2e^- \leftrightharpoons 2B + H_2 \tag{1}$$

For a protic acid, BH^+, under 1.0 atm H_2, the equilibrium thermodynamic potential, $E^0(BH^+/B;H_2)$, of reaction 1 depends on the acid used. In the case of $[Ni(P^{R}_2N^{R'}_2)_2]^{2+}$ catalysts, there are many different possible catalytic pathways.[2] One of our goals is to identify the most favorable pathway and understand the factors controlling the rate-limiting step(s) and the overpotential. The overpotential is the difference between the potential at which catalysis is observed, E, and the equilibrium thermodynamic potential, $E^0(BH^+/B;H_2)$.[54] The latter depends upon the pK_a of the acid BH^+, as shown in eq 2,[55]

$$E^0(BH^+/B;\ H_2) = E^0(H^+/H_2) - 2.303\frac{RT}{F}\,pK_a(BH^+) \tag{2}$$

where $E^0(H^+/H_2)$ is the potential of the standard hydrogen electrode in acetonitrile (−0.028 V vs ferrocenium/ferrocene couple, Fc^+/Fc^0),[22] F is the Faraday constant, R is the ideal gas constant, and T is the absolute temperature. Deviations from eq 2 are expected in the case of aggregation phenomena, such as homoconjugation of the acid with its conjugate base.[22]

We start by analyzing the possible catalytic pathways accessible to evolution of H_2 from acetonitrile solutions of protonated *N*,*N*-dimethylformamide ($[(DMF)H]^+$, $E^0(DMFH^+/DMF;H_2)$ = −0.386 V catalyzed by $[Ni(P^{Ph}_2N^{Ph}_2)_2]^{2+}$.[22] Then catalysis in different acidic media will be explored and implications on rate (turnover frequency, TOF), and overpotential will be discussed. We conclude by outlining the path forward for extending this study to other $[Ni(P^{R}_2N^{R'}_2)_2]^{2+}$ catalytic platforms.

We adopted the following computational approach. First, we performed an extensive study of the elementary reaction steps connecting possible reaction intermediates by using hybrid quantum mechanics/molecular mechanics (QM/MM) molecular dynamics (MD) and standard QM optimization of stationary points on the potential energy surface. These calculations provided thermodynamic and kinetic parameters upon which we built a detailed microkinetic model. The model was validated against available electrochemical data and was then used to infer mechanistic information. Finally, this information was extended to different catalytic conditions (e.g., strength and concentration of the acid used for catalysis and applied electrode potential) by using Polanyi-like linear free energy relationships for activation barriers based on computed reaction free energies.

Reaction Pathways. The overall catalytic activity is determined by a complex sequence of chemical steps that involves electron transfers, intramolecular and intermolecular proton transfers, and association/dissociation of a base or acid to the Ni complex. For a given catalyst, the order of these

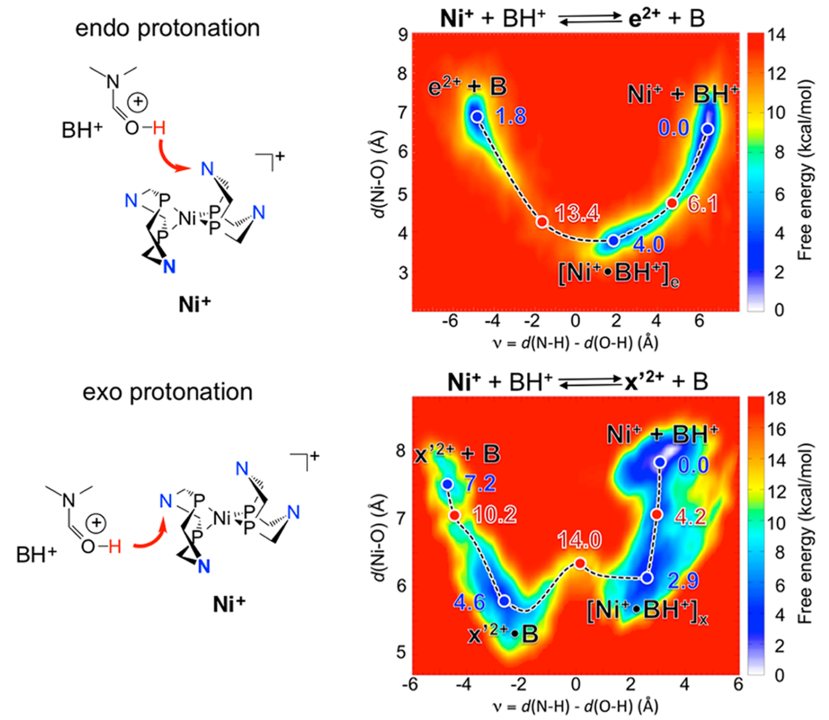

Figure 3. Free energy landscape for endo protonation (top panel) and exo protonation (lower panel) of the $[Ni(P^{Ph}_2N^{Ph}_2)_2]^+$ intermediate, **Ni**$^+$, by $[(DMF)H]^+$ in acetonitrile as obtained from QM/MM metadynamics simulations. The *x*-axis represents the asymmetric stretching coordinate defined by the N atom of the target pendant amine, the $[(DMF)H]^+$ protic H atom, and the O atom of $[(DMF)H]^+$, $\nu = d(N{-}H) - d(O{-}H)$; the *y*-axis represents the distance between the O atom of $[(DMF)H]^+$ and the Ni center, $d(Ni{-}O)$.

events depends on the catalytic conditions, in particular on the strength of the exogenous acid (base), its concentration, and the applied potential. We have performed an exhaustive characterization of the possible elementary steps occurring during H_2 production by $[Ni(P^{Ph}_2N^{Ph}_2)_2]^{2+}$ from acetonitrile solutions of $[(DMF)H]^+$ using previously published data,[19,21,33,34] complemented by new calculations as described in detail in the section on Computational Methods. Briefly, intramolecular chemical events (i.e., proton transfer and conformational changes) were studied using standard quantum chemical calculations based on optimization of stationary points, harmonic corrections to the free energy, and a continuum description of the solvent. Chemical events that are difficult to represent with a continuum description of the solvent and hamornic free energies, such as acid/base association and dissociation, were investigated by QM/MM MD simulations. Possible elementary steps were combined to obtain the lowest-free energy pathway. The structures of all of the main species considered in the present study are provided in Figure S1.

As an example of such an approach, Figure 3 shows the free energy landscape for the protonation of the Ni(I) intermediate by $[(DMF)H]^+$ to the endo site (**Ni**$^+$ + $[(DMF)H]^+$ ⇆ **e**$^{2+}$ + DMF) and the exo site (**Ni**$^+$ + $[(DMF)H]^+$ ⇆ **x**$'^{2+}$ + DMF) obtained from QM/MM simulations. The corresponding canonical free energy profiles are shown in Figure 4. Endo protonation is characterized by two elementary steps (association of the acid, followed by a concerted proton transfer to the pendant amine and dissociation of the conjugate base), whereas the exo protonation requires four elementary steps (association/dissociation events, proton transfer, and chair/boat interconversion). A detailed discussion of these elementary steps was presented previously.[33] Here, we stress that exo protonation leads to pinched structures and requires chair/boat isomerization of one of the six-membered rings that include the phosphine ligand and the metal center. Isomerization of nonpinched forms (indicated with a prime in Figure 3 and Figure 4, e.g., **x**′; see Figure S1 for the structure) can take place at any elementary step along the protonation pathway or even before association of the catalyst with the acid. Figure 4 shows the lowest-energy pathway, in which the ring inversion

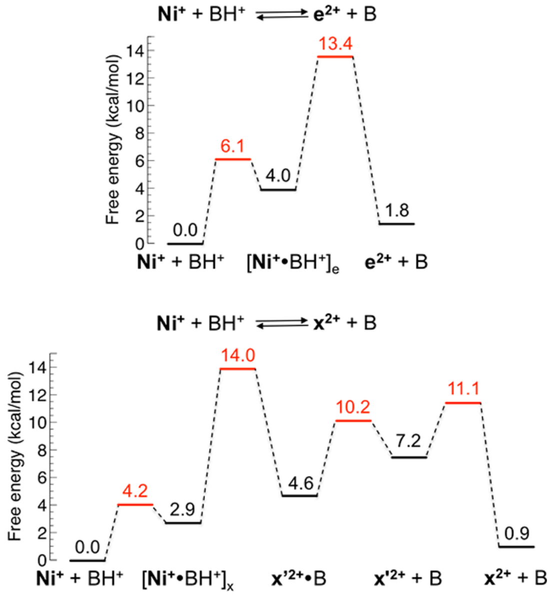

Figure 4. Lowest free energy pathway for endo (top panel) and exo (bottom panel) protonation of the $[Ni(P^{Ph}_2N^{Ph}_2)_2]^+$ intermediate, **Ni**$^+$, by $[(DMF)H]^+$ in acetonitrile.

takes place after dissociation of DMF from $\mathbf{x}'^{2+}$. In the present case, we found that the ring inversion in the association complex catalysts/base has an appreciably high barrier (see Supporting Information).

Free energy landscapes and profiles for other possible chemical reactions are shown in the Supporting Information. Putting all this information together, a refined version of the catalytic mechanism presented in Figure 2 was elaborated and is shown schematically in Figure 5. In the mechanism reported in Figure 5, in addition to the ECEC pathways reported in Figure 2, EECC pathways have also been considered. A discussion of the role of each possible pathway on catalysis is presented below.

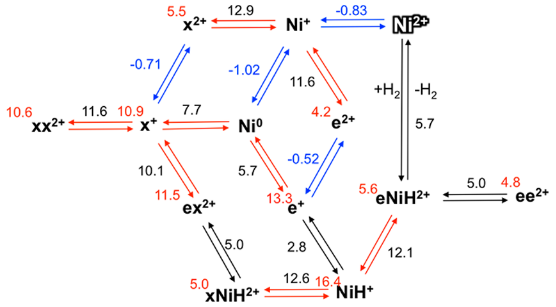

Figure 5. Kinetic model considered in the present study for H_2 production from $[(DMF)H]^+$ in acetonitrile catalyzed by $[Ni(P_2^{Ph}N_2^{Ph})_2]^{2+}$ (indicated with the shadowed label $\mathbf{Ni^{2+}}$). The structure of the various intermediates is given in Figure 2 and Figure S1. Intermolecular protonation/deprotonation reactions (red arrows) are composed of multiple elementary reactions. Each endo protonation reaction is composed of two elementary steps (see, for instance, Figure 4), whereas each exo protonation is composed of at least four elementary steps (see Figures 4, S2, S3, and S4). Blue and black arrows indicate electron transfer and intramolecular reorganization processes, respectively. For each thermochemical reaction, the overall activation barrier (kcal/mol) in the direction of the arrow is reported in black. The pK_a value of the various N-protonated species is reported in red. Reduction potentials are reported in blue (in V vs the Cp_2Fe^+/Cp_2Fe^0 couple in acetonitrile). All data reported are from computational results. For a detailed discussion of the model, see the Computational Methods section. For clarity, in the chemical equation of protonation/deprotonation reactions, the acid and the conjugate base are omitted.

Microkinetic Model. A microkinetic analysis was performed to validate the reactions network reported in Figure 5 and to assess the role of the various possible pathways on catalysis. A detailed description of such an analysis is reported in the Computational Methods section. Briefly, kinetic and diffusion equations were solved using kinetic parameters obtained from ab initio calculations and diffusion coefficients obtained from classical MD simulations (Tables S1, S2). Electron transfer was described in terms of Butler−Volmer kinetics with heterogeneous standard electron transfer rates inferred from experimental electrochemical measurements on $[Ni(P_2^RN_2^{R'})_2]^{2+}$ complexes. It is known that $[(DMF)H]^+$ undergoes homoconjugation,[22]

$$[(DMF)H]^+ + DMF \leftrightarrows [(DMF)_2H]^+ \quad K_{homo} = 49\ M^{-1} \tag{3}$$

so homocojugation is included in our kinetic model.

On the basis of the reaction network reported in Figure 5, we performed simulations of cyclic voltammograms (CVs) and compared them with the experimentally measured CVs. Figure 6a (black dashed line) shows the simulated catalytic current for [cat] = 0.43 mM and $[(DMF)H^+]$ = 0.22 M. As can be seen, the simulated CV shows catalytic currents are smaller than the experimentally measured currents (red line). Similar results are obtained for other acid concentrations. This indicates that our kinetic model underestimates catalytic TOFs.

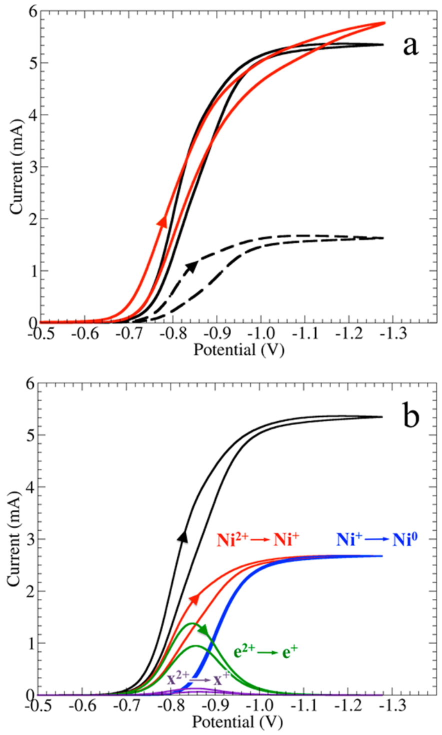

Figure 6. Cyclic voltammogram (CV) for H_2 production from 0.22 M solution of $[(DMF)H]^+$ in acetonitrile catalyzed by 0.43 mM $[Ni(P_2^{Ph}N_2^{Ph})_2]^{2+}$ (potential scan rate = 50 mV/s, electrode surface 1 cm^2). Panel a: calculated CV (dashed line, from the raw ab initio kinetic parameters; solid line, after fitting of selected protonation barriers) vs experimental CV (red line, with the current scaled to the electrode area of 1 cm^2). Panel b: Decomposition of the total current into the most important contributing redox processes. The applied potential is reported with respect to the Cp_2Fe^+/Cp_2Fe^0 couple. More details on the current decomposition are provided in Figure 9.

Considering the number of the chemical steps that contribute to the overall rate of H_2 production, the agreement between calculated and experimental CVs should be considered satisfactory. However, to go a step further and understand which reactions are responsible for the discrepancy between simulated and experimental CVs and, at the same time, obtain preliminary mechanistic insights from our kinetic model, a sensitivity analysis was carried out. Specifically, we investigated the dependence of the rate of production of H_2 on the various rate constants defining the microkinetic model. To this end, we calculated the derivative of the concentration of H_2 at the electrode surface (x = 0) with respect to the forward rate constant, $\vec{k}_i$, for every reaction i:

$$f_i(H_2) = \frac{1}{[\mathrm{cat}]} \frac{\partial [H_2]_{x=0}}{\partial \vec{k}_i}$$

keeping all the other forward rate constants $\vec{k}_j$ with $j \neq i$ and reverse rate constants fixed. Clearly, in the case of the protonation reactions in which all the intermediates are higher in energy than the initial and final state (e.g., Figure 4), this sensitivity analysis does not allow the contributions due to the rate-limiting step (kinetic effects) and the pre-equilibria (thermodynamic effects) to be disentangled. For these reactions, it is also evident that an analysis of the variation of the H_2 production with respect to other possible parameters, such as the equilibrium constants, does not allow discriminating kinetic from thermodynamic steps. For this reason, the analysis was carried out using an effective rate constant, defined in terms of the highest point along the free energy path.

We identified four chemical reactions that have the greatest influence on the rate of production of H_2 at the electrode surface. These steps are the endo and exo protonation of the Ni(I) and the Ni(II) hydride intermediates, that is, $\mathbf{Ni^+}$ and $\mathbf{NiH^+}$; their relative contribution varies with the applied potential (Figure 7). Figure 7 shows that the rate of formation of H_2 is more sensitive to the protonation of $\mathbf{NiH^+}$ than $\mathbf{Ni^+}$. All of the other reactions in the model of Figure 5 influence the rate at the electrode surface by at least 1 order of magnitude less than these four processes. This finding represents important mechanistic information. The branching points offered by the protonation of the nonprotonated Ni(I) species and the Ni(II) hydride ($\mathbf{NiH^+}$) have a pivotal role in catalysis. We will elaborate this role below. Here, we will focus on improving and further validating the kinetic model to allow for a comparison with the experimental data as closely as possible.

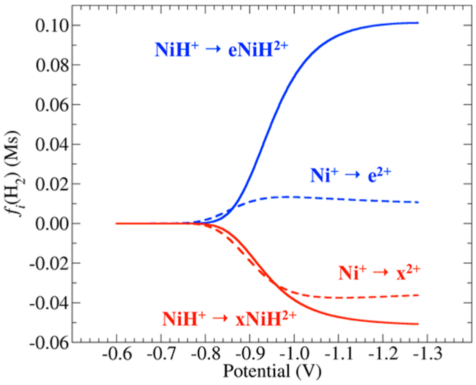

Figure 7. Sensitivity analysis for H_2 production at the electrode surface from 0.22 M solution of $[(DMF)H]^+$ in acetonitrile catalyzed by 0.43 mM $[Ni(P_2^{Ph}N_2^{Ph})_2]^{2+}$ as a function of the applied potential (vs Cp_2Fe^+/Cp_2Fe^0). See the caption to Figure 6 for further details.

Our analysis suggests that protonations of $\mathbf{Ni^+}$ and $\mathbf{NiH^+}$ are important processes, but with the present model, we cannot identify which elementary step (or combination of steps) is the most important (a pre-equilibrium or the rate-determining step). With this in mind, we then performed an optimization of the activation barrier of the rate-determining steps for the four protonation reactions to reproduce the best fit with the experimental CV of Figure 6, in terms of least-squares agreement. The result of such a fit is reported in Figure 6a (black solid line). We found that small changes in the activation barriers of these steps have a large influence on the CV. For instance, the barrier for the $[\mathbf{Ni^+}{\cdot}BH^+]_e \rightarrow \mathbf{e^{2+}} + B$ step was reduced by 1.8 kcal/mol, whereas the barrier for the $[\mathbf{Ni^+}{\cdot}BH^+]_x \rightarrow \mathbf{x'^{2+}}{\cdot}B$ step was reduced by only 1.1 kcal/mol. Because of these small changes and the marked improvement between simulated and experimental CV, the discussion presented in the following sections uses these "optimized" barriers.

We conclude this section further discussing the reliability of the kinetic model by calculating the TOF for different acid concentrations and comparing it with the experimental values. The TOF was calculated following the same method adopted experimentally.[17] The procedure is based on a well-established formula[56−58] that expresses the TOF in terms of the catalytic current, i_{cat}, and the peak current for the Ni(II/I) wave in the absence of acid, i_p (eq 4),

$$\mathrm{TOF} = \left(\frac{0.04463}{n}\right)^2 \frac{F\upsilon}{RT}\left(\frac{i_{cat}}{i_p}\right)^2 \tag{4}$$

where n is the number of electrons involved in the catalytic production of H_2, and υ is the scan rate in volts per second. As for the experimental determination of the TOF, we took i_{cat} at the most positive potential for each simulated catalytic wave beyond $E_{1/2}$ of the Ni(II/I) couple (−0.83 V vs Cp_2Fe^+/Cp_2Fe^0) for which the second derivative of the current with respect to the potential is zero.

Experimental TOFs are available for both unbuffered $[(DMF)H]^+$ solutions and for 1:1 $[(DMF)H]^+$/DMF buffered acid solutions.[34] Consequently, calculations were carried out for both solutions at various acid concentrations. As can be seen from the results reported in Figure 8a, the agreement between simulation (solid lines) and experiment (circles) is excellent, which makes us confident that our model is sufficiently accurate to quantitatively describe the mechanism for H_2 evolution catalyzed by $[Ni(P_2^{Ph}N_2^{Ph})_2]^{2+}$. We will analyze the dependence of the TOF on the acid concentration in the following sections.

Catalytic Pathways. In this section, we present an analysis of the most probable catalytic pathways and the factors limiting catalysis. We start by analyzing the various redox processes contributing to the total catalytic current. The kinetic model of Figure 5 comprises four distinct redox processes (indicated with blue arrows), each of them contributing to the total current. These processes are the reduction of the non-protonated Ni(II) and Ni(I) species, (1) $\mathbf{Ni^{2+}} + e^- \rightarrow \mathbf{Ni^+}$ and (2) $\mathbf{Ni^+} + e^- \rightarrow \mathbf{Ni^0}$, and the reduction of the endo and exo singly protonated Ni(I) species, (3) $\mathbf{e^{2+}} + e^- \rightarrow \mathbf{e^+}$ and (4) $\mathbf{x^{2+}} + e^- \rightarrow \mathbf{x^+}$. A decomposition of the current in these elementary contributions indicates that the relative weight of the four reduction reactions depends on the applied potential (Figure 6b). At more positive potentials the major contribution comes from the $\mathbf{Ni^{2+}} + e^- \rightarrow \mathbf{Ni^+}$ and $\mathbf{e^{2+}} + e^- \rightarrow \mathbf{e^+}$ processes, with a minor contribution from the $\mathbf{x^{2+}} + e^- \rightarrow \mathbf{x^+}$ reduction. As we sweep the potential to more negative values, the $\mathbf{e^{2+}} + e^- \rightarrow \mathbf{e^+}$ process diminishes, and the $\mathbf{Ni^+} + e^- \rightarrow \mathbf{Ni^0}$ process becomes predominant.

These results clearly show that the catalytic pathway depends on the applied potential (Figure 6b). At the onset of the catalytic current, the preferential pathway corresponds to an ECEC process in which the Ni(II) complex is first reduced and then protonated to form either the $\mathbf{e^{2+}}$ or $\mathbf{x^{2+}}$ intermediates, which are, in turn, further reduced. Consistent with the calculated barriers for endo and exo protonation of the Ni(I) intermediate (Figure 4), Figure 6b indicates that endo protonation is preferred over exo protonation. On the other hand, at more negative potentials, the preferred pathway is an EECC process where the Ni(II) complex is reduced to Ni(I) and then to Ni(0). The maximum contribution from the ECEC is reached at the Ni(II/I) potential, $E^0(\mathbf{Ni^{2+}}/\mathbf{Ni^+}) = -0.840$ V.

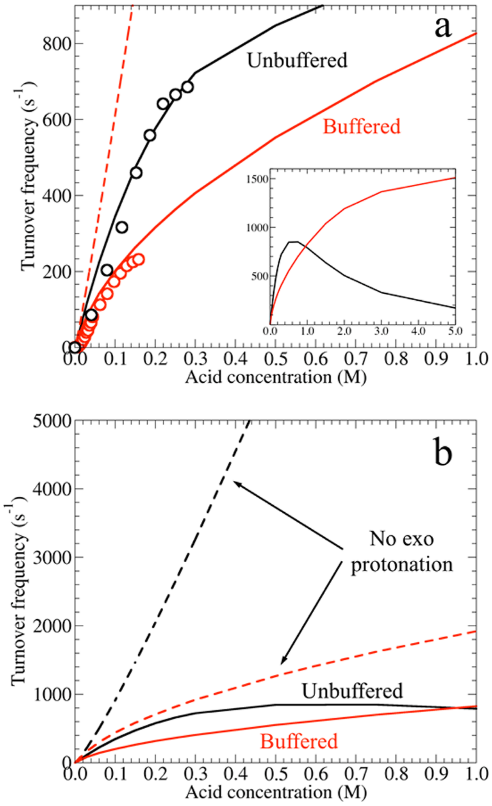

Figure 8. Calculated turnover frequencies as a function of the concentration unbuffered $[(\mathrm{DMF})\mathrm{H}]^+$ and 1:1 $[(\mathrm{DMF})\mathrm{H}]^+/\mathrm{DMF}$ buffered acid acetonitrile solutions. (a) Calculated (solid lines) vs experimental values (circles);[17] the dashed line represent the TOF for the buffered solution with the acid concentration scaled to take into account the homoconjugation effects; the inset shows the calculated values over a wider range of acid concentrations. (b) Calculated values with the exo protonation channel shut down.

At the applied potential of about −0.890 V, the $\mathbf{e^{2+}} + \mathrm{e^-} \rightarrow \mathbf{e^+}$ and $\mathbf{Ni^+} + \mathrm{e^-} \rightarrow \mathbf{Ni^0}$ reactions equally contribute to the total current; consequently, the ECEC and EECC pathways equally contribute to the catalytic turnover. At the potential at which the turnover frequency is measured (E = −0.995 V), the contributing process is mostly the EECC pathway. Additional important information provided by Figure 6b is that the ECEC pathway features slower catalytic rates than the EECC pathway, but it operates at lower overpotential.

A pictorial representation is provided in Figure 9, where the total reaction fluxes in the catalyst diffusion layer are reported for three different potentials. The reaction fluxes of Figure 9 indicate the amount of substance transformed per unit of time in the diffusion layer in the direction of the transformation. For instance, the flux of the reaction $\mathbf{Ni^+} + [(\mathrm{DMF})\mathrm{H}]^+ \leftrightarrows \mathbf{e^{2+}} + \mathrm{DMF}$ at distance x from the electrode surface is defined as

$$\emptyset(\mathbf{Ni^+} \rightarrow \mathbf{e^{2+}}; x) = \vec{k}[\mathbf{Ni^+}]_x[\mathrm{DMFH^+}]_x - \overleftarrow{k}[\mathbf{e^{2+}}]_x[\mathrm{DMF}]_x$$

where $\vec{k}$ and $\overleftarrow{k}$ are the forward and reverse reaction constants. Integration of $\emptyset(\mathbf{Ni^+} \rightarrow \mathbf{e^{2+}};x)$ over the thickness of diffusion layer ($L \sim (Dt)^{1/2}$, where D is the diffusion coefficient of the catalyst) yields the total chemical flux for the reaction. As can be seen, the reduction of the $\mathbf{Ni^{2+}}$, $\mathbf{Ni^+}$, and $\mathbf{e^{2+}}$ species and the intramolecular proton transfer reactions (e.g., migration of the proton from the endo N-protonated Ni(0) intermediate to the Ni(II) hydride, $\mathbf{e^+} \rightarrow \mathbf{NiH^+}$) have the largest fluxes. As expected from the calculated activation barrier presented above, intermolecular protonation (deprotonation) reactions by $[(\mathrm{DMF})\mathrm{H}]^+$ (DMF) have the smallest flux. From the analysis of the reaction flux, it is also evident that the endo protonation of the Ni(II) hydride, $\mathbf{NiH^+} + [(\mathrm{DMF})\mathrm{H}]^+ \leftrightarrows \mathbf{eNiH^{2+}} + \mathrm{DMF}$, which is a common step to both ECEC and EECC mechanisms, is the rate-limiting process, presenting the smallest flux. It is also worth pointing out how the flux for endo (and, to a lesser extent, exo) protonation of the Ni(0) intermediate is highly dependent on potential because the concentration of this intermediate, which results from the sequential two-electron reduction of the Ni(II) species, also depends on the applied potential. Figure 9 also shows that, under catalytic conditions, appreciable amounts of the exo protonated species are formed. These intermediates are not part of the highest reaction flux pathways for H_2 production, and it is of interest to analyze how, and to what extent, their formation affects catalysis. This is analyzed in the next section.

Exo Protonation and Acid Concentration Dependence. The analysis of the reaction flux shows that the pathways leading to H_2 evolution have the highest flux. In the catalytic conditions of Figure 9 at E = −0.995 V, the endo protonation EECC pathway has a flux of 2.4 M s^{-1}, whereas the ECEC has a flux of 0.6 M s^{-1}; however, Figure 9 shows that pathways leading to $\mathbf{xNiH^{2+}}$ and $\mathbf{xx^{2+}}$ also exist. Although these species are thermodynamically unstable toward release of H_2 by about 7 and 10 kcal/mol, respectively, with regeneration of the catalyst, they are kinetically populated. At E = −0.995 V, the total chemical flux leading to $\mathbf{xNiH^{2+}}$ and $\mathbf{xx^{2+}}$ is 0.6 and 0.2 M s^{-1}, respectively. The quantity of the $\mathbf{xNiH^{2+}}$ and $\mathbf{xx^{2+}}$ intermediates formed depends on the applied potential (Figure S5), being $\mathbf{xNiH^{2+}}$ dominant below E = −0.890 V, the potential at which ECEC and EECC pathway are equally probable.

To understand the role of exo protonation, we repeated the simulation of the CV with all exo protonation reactions removed from the kinetic model. The results reported in Figure 8b clearly show that the catalytic rates in absence of exo protonation are markedly higher. As illustrated in Figure S6, the protonation events leading to $\mathbf{xx^{2+}}$ have the largest influence on the TOF, with a major penalty coming from protonation of the $\mathbf{x^+}$ intermediate. The protonation events leading to $\mathbf{xNiH^{2+}}$ have a smaller but still important effect on the TOF, with the major contribution coming from the protonation of the Ni(II) hydride intermediate. Exo protonation is also key for understanding the dependence of the TOF on the concentration of $[(\mathrm{DMF})\mathrm{H}]^+$ reported in Figure 8. Catalytic rates increase with higher acid concentrations up to a concentration of $[\mathrm{DMFH^+}]$ = 0.6 M, after which adding more acid decreases the rate (Figure 8b, inset). This behavior can be easily explained looking at the dependence of the concentration of the three critical intermediates $\mathbf{NiH^+}$, $\mathbf{xNiH^{2+}}$ and $\mathbf{xx^{2+}}$ as a function of the acid concentration (Figure 10). As can be seen, at the potential at which the TOF is measured (−0.995 V), for $[\mathrm{DMFH^+}] < 0.71$ M, the dominant species at the electrode surface is $\mathbf{NiH^+}$; however, beyond this acid concentration, the dominant species becomes $\mathbf{xNiH^{2+}}$, and the TOF decreases. Although at low acid concentration, $\mathbf{NiH^+}$ is the dominant species at the electrode surface, the exo protonated intermediates $\mathbf{xx^{2+}}$ and $\mathbf{xNiH^{2+}}$ are the dominant protonated species in the diffusion layer, as illustrated in Figure S7. The $\mathbf{xx^{2+}}$ species accumulates in the diffusion layer because of the high activation barrier for deprotonating it back to the $\mathbf{x^+}$

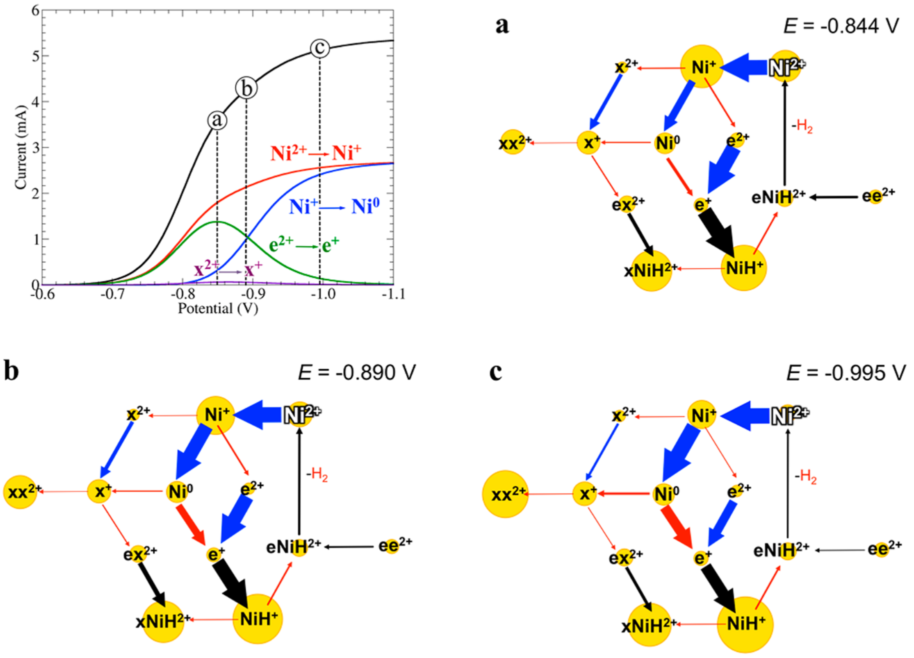

Figure 9. Concentration of various catalytic intermediates (yellow circles) and reaction fluxes (arrows) at three different potentials in a simulated cyclic voltammogram (left, top panel) for H_2 production from a 0.22 M solution of $[(DMF)H]^+$ in acetonitrile catalyzed by 0.43 mM $[Ni(P^{Ph}_2N^{Ph}_2)_2]^{2+}$ (scan rate = 50 mV/s, electrode surface = 1 cm^2): (a) $E = -0.844$ V; (b) $E = -0.890$ V; (c) $E = -0.995$ V. The radius of the circles and the thickness of the arrows are proportional to the logarithm of the molar fraction at the surface and the total reaction flux, respectively. The direction of arrows indicates the direction of the flux. Blue arrows, electron transfer reactions; red arrows, intermolecular proton transfers (from $[(DMF)H]^+$/to DMF); Black arrows, intramolecular proton reorganization and H_2 elimination.

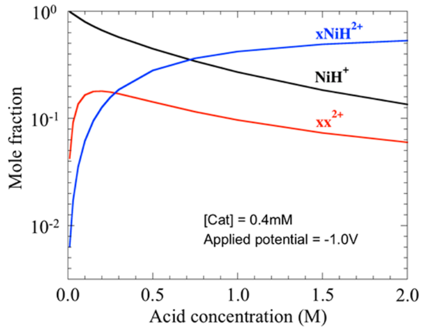

Figure 10. Mole fraction at the electrode surface (see text for the definition) of the most relevant catalytic species as a function of the acid concentration in an unbuffered acid solution at an applied potential $E = -0.995$ V.

intermediate (16.1 kcal/mol) compared with any other proton transfer barrier. Consequently, formation of the $\mathbf{xx}^{2+}$ intermediate has a greater impact on the catalytic rate than expected from the low chemical flux leading to $\mathbf{xx}^{2+}$.

Figure 8 also shows that in a 1:1 $[(DMF)H]^+$/DMF buffered acid solution, catalytic rates increase monotonically with the nominal acid concentration, C_{DMFH^+}. Indeed, the presence of a large excess of base (DMF) facilitates deprotonation of exo isomers, and therefore, endo isomers are always the dominant species. On the basis of this argument, one would have expected higher TOF for a buffered acid solution than an unbuffered acid solution at any acid concentration. This is not the case because of homoconjugation, which considerably reduces the amount of free acid. It can be shown that $[DMFH^+] \propto K_{homo}^{-1}(1 + 4K_{homo}C_{DMFH^+})^{1/2}$. If we report the TOF as a function of the actual amount of free acid in the buffer solution, instead of its nominal concentration, we find, as expected, that in buffered solution, catalysis proceeds much faster than in an unbuffered acid solution (see Figure 8a, red dashed line). We also point out that because of homoconjugation, in the absence of exo protonation, the TOF for unbuffered solutions is still much larger than that for buffered solutions.

We conclude this section pointing out that in the absence of exo protonation, the model of Figure 5 predicts a linear increase of the TOF with acid concentration without reaching saturation in any reasonable range of concentrations (Figure 8). This is observed experimentally for some $[Ni(7P^R_2N^{R'})_2]^{2+}$ catalysts (Figure 1c) in which exo protonation is highly disfavored thermodynamically over endo protonation.[38]

Extension to Different Catalytic Conditions. The model presented above describes the production of H_2 from acetonitrile solutions of $[(DMF)H]^+$ catalyzed by $[Ni(P^{Ph}_2N^{Ph}_2)_2]^{2+}$. In particular, it provides a rationale of how the presence of multiple protonation sites (endo vs exo) influences catalysis. The model predicts that disfavoring exo protonation results in an enhancement of the catalytic rates. The detrimental role of exo protonation was already postulated on the basis of previous experimental and theoretical studies, and discussed previously.[19,33,38,50] This information has been employed to design catalysts with exceedingly high rates for H_2 production.[37,38] The kinetic investigation presented above has allowed for a novel quantitative understanding of the role of exo protonation. In particular, it has pointed out that, although thermodynamically unstable toward the release of H_2, exo protonated Ni(0) species are kinetically stable and slowly accumulate over time. In this section, we will take a step further and infer additional guiding principles to improve catalysis. Most importantly, we will show that the model can be generalized to any $[Ni(P^R_2N^{R'}_2)_2]^{2+}$ catalytic platform and employed along with thermodynamic linear free energy relationships to infer the optimal catalytic conditions toward the design of new synthetic targets.

The model of Figure 5 was built from an exhaustive and time-consuming series of ab initio calculations. Ideally, to extend it to different conditions (e.g., different acids) and complexes, we need to be able to predict kinetic parameters without repeating quantum chemical calculations for each condition and catalyst or by reducing as much as possible the number of calculations to be done. Toward this end, a first dramatic simplification comes from the realization that we do not need to consider all of the elementary steps that are included in the model. It is necessary just to identify the minimal number of chemical transformations that define the microkinetic model that is required to accurately describe catalysis (model reduction).[59,60] Here, we define chemical transformations as a sequence of elementary steps that defines a given process, for example, the overall protonation reactions of the Ni(I) intermediate reported in Figure 4: $\mathbf{Ni}^+ + [(\mathrm{DMF})\mathrm{H}]^+ \leftrightarrows \mathbf{e}^{2+} + \mathrm{DMF}$ and $\mathbf{Ni}^+ + [(\mathrm{DMF})\mathrm{H}]^+ \leftrightarrows \mathbf{x}^{2+} + \mathrm{DMF}$. A model defined in terms of this minimal set of reactions is called macrokinetic model. For the present case, the macrokinetic model describing the catalytic evolution of H_2 by $[\mathrm{Ni}(\mathrm{P}_2^{\mathrm{Ph}}\mathrm{N}_2^{\mathrm{Ph}})_2]^{2+}$ is clearly given by the simplified reaction network of Figure 5, which defines the catalytic cycle. Indeed, using this model with kinetic parameters inferred from the overall activation barriers dictated by the sequences of elementary steps discussed above, we obtain TOFs very similar to those reported in Figure 8, the differences being within a few percent. The next step is to devise a way to predict these barriers using easily accessible parameters. We outline here a possible method to achieve this goal.

Suppose we want to predict the effect of the strength of the acid employed. In this case, the reactions we need to focus on are the protonation/deprotonation steps that define the macrokinetic model. As expected for a series of homologous reactions, the Bell−Evans−Polanyi principle[61,62] applies fairly well to the present case. Protonation free energies, ΔG^0, and associated barriers, $\Delta G^{\ddagger}$, show a reasonably good linear correlation (Figure S8). A linear regression yields the following equation,

$$\Delta G^{\ddagger} = 0.59\Delta G^0 + 12.1\ \mathrm{kcal/mol} \tag{5}$$

(correlation coefficient $R^2 = 0.92$ and standard error of the coefficients of 9.7×10^{-2} and 0.69 kcal/mol, respectively). The reaction free energy can be easily obtained from the pK_a values of the protonated catalytic intermediate, i, and the exogenous acid, BH^+:

$$\Delta G^0 = \ln(10)RT(\mathrm{p}K_\mathrm{a}^{\mathrm{BH}^+} - \mathrm{p}K_\mathrm{a}^{i})$$

Using these simple relationships, we can interrogate the macrokinetic model of Figure 5 to determine the optimal strength of the acid and its concentration that maximizes the catalytic rate and minimizes the overpotential. However, the extension of the model in Figure 5 to different acidic media requires additional considerations. The first consideration is that eq 5 was derived for the $[\mathrm{Ni}(\mathrm{P}_2^{\mathrm{Ph}}\mathrm{N}_2^{\mathrm{Ph}})_2]^{2+}/[(\mathrm{DMF})\mathrm{H}]^+$ catalytic system. If we want to use it to explore different acidic media, it is important to assess its transferability. Figure S8 shows the comparison between the $[\mathrm{Ni}(\mathrm{P}_2^{\mathrm{Ph}}\mathrm{N}_2^{\mathrm{Ph}})_2]^{2+}/[(\mathrm{DMF})\mathrm{H}]^+$ and $[\mathrm{Ni}(\mathrm{P}^{\mathrm{Cy}}{}_2\mathrm{N}^{\mathrm{Me}}{}_2)_2]^{2+}/\mathrm{PhNH}_3^+$ systems (where Cy = cyclohexyl, Me = methyl), extensively discussed previously.[19,33,34] As can be seen, the latter also show a good linear correlation between activation barriers, $\Delta G'^{\ddagger}$, and reaction free energies:

$$\Delta G'^{\ddagger} = 0.57\Delta G^0 + 18.8\ \mathrm{kcal/mol} \tag{6}$$

(correlation coefficient $R^2 = 0.95$; standard error of the coefficients 1.0×10^{-1} and 0.49 kcal/mol, respectively).

Equations 5 and 6 show similar slopes (0.59 vs 0.57) but different intercepts (12.1 vs 18.8 kcal/mol). Protonation of $[\mathrm{Ni}(\mathrm{P}_2^{\mathrm{Cy}}\mathrm{N}_2^{\mathrm{Me}})_2]^{2+}$ catalytic intermediates by PhNH_3^+ is considerably more difficult because of steric penalties associated with the size of the Cy substituents and PhNH_3^+. The different intercepts in the two equations are a reflection of the different steric contributions in the two systems. Instead, the contributions due to a mere difference in acidity (i.e., $\mathrm{p}K_\mathrm{a}^{\mathrm{BH}^+} - \mathrm{p}K_\mathrm{a}^{i}$) are comparable, as indicated by the similar slopes. As a consequence, linear free energy relationships for protonation reactions should be parametrized accounting for the steric properties of the system. This necessitates further calculations that are beyond the scope of this paper. In what follows, we will use eq 5. Therefore, the results should be considered valid for catalytic systems with steric properties similar to $[\mathrm{Ni}(\mathrm{P}_2^{\mathrm{Ph}}\mathrm{N}_2^{\mathrm{Ph}})_2]^{2+}/[(\mathrm{DMF})\mathrm{H}]^+$. Nevertheless, the results are of general qualitative validity, and they provide important mechanistic insights into how the acid strength influences catalysis while keeping other factors (sterics) constant. To make a direct comparison with the results reported in the sections above, we initially assume that when changing the strength of the acid, its propensity for homoconjugation does not change. The role of homoconjugation is discussed in the Supporting Information.

A second issue we need to take into account to extend the kinetic analysis to other acids is the possibility of introducing additional pathways as we change the strength of the external acid. Indeed, although protonation of Ni^{2+} is negligible with $[(\mathrm{DMF})\mathrm{H}]^+$ (e.g., the pK_a value of the endo protonated Ni(II) intermediate, $\mathbf{e}^{3+}$, is about about 1), it could become possible using stronger acids. Therefore, the analysis of the effect of the strength of the protonating agent was carried out including this possibility. The extended kinetic model is shown in Figure S9, and it includes the formation of singly and doubly protonated Ni(II) species as well as doubly protonated Ni(I) species (CECE, CCEE, and ECCE pathways). We emphasize that the extended model of Figure S9 assumes H_2 elimination from $\mathbf{eNiH}^{2+}$. However, in strong acidic media, H_2 evolution could also occur from triply protonated species, such as $\mathbf{eeNiH}^{3+}$. We are currently exploring this possibility, and it has not been considered in the present study. The structure of all of the species considered in the extended model is given in Table S1. The pK_a values of the additional species introduced in the extended model were calculated from previously reported linear free energy relationships for thermodynamic quantities.[2]

We present below the results obtained from the extended macrokinetic model given in Figure S9, focusing on the dependence of the catalytic pathways, TOF, and overpotential on the strength of the acid employed for catalysis. A discussion on how the homoconjugation constant of the acid with its conjugate base influences catalysis is provided in the Supporting Information.

Turnover Frequency and Acid Strength. The turnover frequency as a function of the acid concentration and strength calculated from the extended model discussed above is given in

Figure 11 for both unbuffered acid solutions and 1:1 BH^+/B buffered acid solutions. Figure 11a shows that, in unbuffered acid solutions, for a given acid strength, there is a corresponding optimal acid concentration for which the TOF is at maximum. This result is due to the balance between endo and exo protonation. The rate of protonation increases with the strength and the concentration of the exogenous acid. However, as discussed earlier, at high acid concentration, exo protonated species become dominant and cause a decrease in the TOF. Similarly, increasing the strength of the acid favors the production of exo isomers. The concentration threshold at which the exo isomers become predominant decreases as the $pK_a^{BH^+}$ decreases. The proposed model indicates that the highest rate of H_2 production is achieved for $pK_a^{BH^+} = 4.3$ and $[BH^+] \approx 0.07$ M. Under these conditions, the calculated TOF is ≈1160 s^{-1}, which should be compared to the calculated TOF ≈ 861 s^{-1} with 0.6 M $[(DMF)H]^+$ ($pK_a = 6.1$).

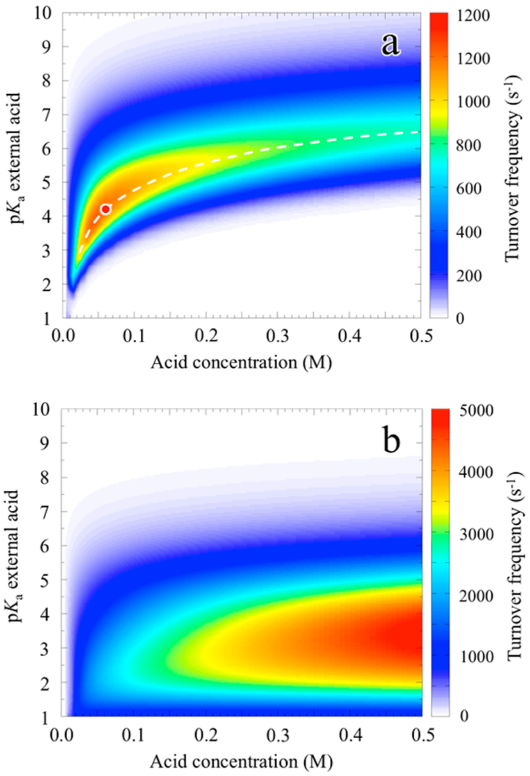

Figure 11. Dependence of the turnover frequency on the concentration and strength of the acid used for catalysis. (a) Nonbuffered acid solutions; (b) 1:1 BH^+/BH buffered acid solutions. TOFs were taken at the most positive potential for each simulated cyclic voltammetry experiment beyond $E_{1/2}$ of the Ni(II/I) couple for which the second derivative of the current with respect to the potential is zero. See Figure 8 for further details.

In contrast, in buffered acid solutions, addition of higher concentrations of acid is not detrimental because the excess of conjugate base facilitates the conversion of the exo isomers to endo isomers. Therefore, rates increase with the acid concentration without reaching a saturation regime at any experimentally achievable concentration. On the other hand, increasing the acid strength increases the rate of endo protonation, which leads to an increase in the TOF. However, the rate of exo protonation also increases and, beyond a given concentration threshold, exo isomers become predominant and the TOF drops.

Catalytic Pathways. In $[(DMF)H]^+$ solution, two types of pathways are operative. The analysis of the reaction flux showed that for potentials more positive than −0.89 V, the major contribution to the catalytic rate comes from the ECEC pathways, where the Ni(II) complex is first reduced, then protonated, reduced, and finally, protonated again. For potentials more negative than −0.89 V, the major contribution comes from the EECC pathways where the Ni(II) is sequentially reduced to Ni(I), then Ni(0), and then protonated. In Figure 12, we report the result of a similar analysis for the extended model of Figure S9. For the extended model, there are a total of six major types of pathways (EECC, ECEC, ECCE, CEEC, CECE, and CCEE), with various possibilities within each category, depending on the endo and exo protonation/deprotonation sequence.

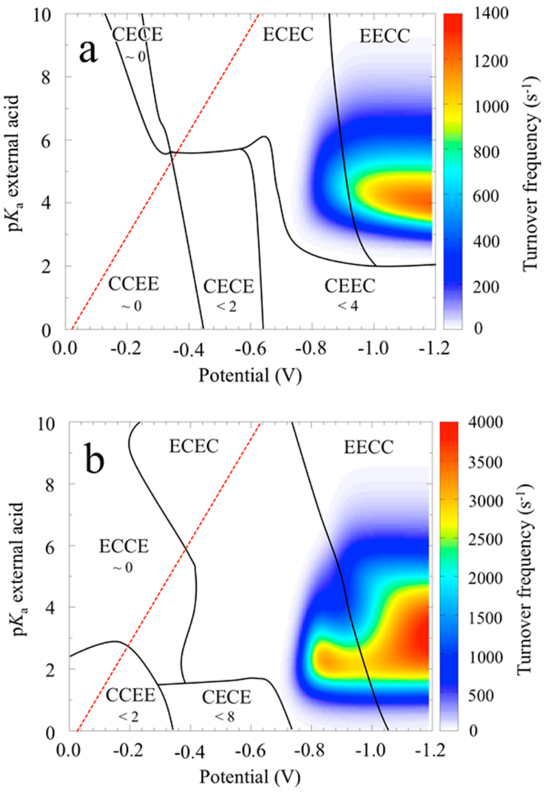

Figure 12. Dependence of the turnover frequency on the strength of the exogeneous acid and the applied potential. (a) 0.1 M acid solution; (b) 0.61 M BH^+/B buffered solution (actual concentration of free acid $[BH^+] = 0.1$ M). Potential is changed at a scan rate of 50 mV/s. The diagrams are divided into zones according to the predominant pathway operating at a given potential and pK_a of the external acid. The number given below the CCEE, CECE, and ECCE labels indicates explicitly the highest turnover frequency (s^{-1}) for that pathway, which is too small to be visible on the color scale of the contour plots. The dashed red line denotes the standard state thermodynamic potential of the acid BH^+.

Figure 12 shows data for both 0.1 M unbuffered acid solution (part a) and 0.61 M buffered acid solution (part b). The latter corresponds to a concentration of free acid in solution of 0.1 M for a homoconjugation constant $K_{homo} = 49\ M^{-1}$,[22] which allows for a direct comparison between nonbuffered and buffered conditions. The TOFs reported in Figure 12 are calculated using eq 4, with the current taken at a given potential, not at the most negative potential for which the second derivative of the current with respect to the potential is zero, as for the TOF (i_{cat}) discussed in the previous sections. The two diagrams are divided into zones according to the predominant pathway operating at a given potential and strength of the acid. High TOFs are observed only when either the ECEC or EECC pathways become operative. Depending on the solution conditions (unbuffered or 1:1 BH^+/B buffered acid solution), the onset of these pathways varies with the strength of the acid and the applied potential. Other possible alternative pathways, where catalysis is initiated by preprotonation of the Ni(II) species, are dominant at more positive potentials of the ECEC pathways or in more acidic media. However, the TOFs achievable via these pathways are very small. In the case of (unbuffered) acid solution, sizable TOFs are observed only for CECE and CEEC pathways (TOF < 2 and 4 s^{-1}, respectively). In buffered solutions, appreciable TOFs are observed for the CCEE and CECE pathways (TOF < 2 and 8 s^{-1}, respectively). All these pathways are accessible at low $\mathrm{p}K_\mathrm{a}$ values of the medium.

Overpotential. For the $[\mathrm{Ni}(\mathrm{P}_2^{\mathrm{Ph}}\mathrm{N}_2^{\mathrm{Ph}})_2]^{2+}$ catalyst, the onset of significant catalytic currents is determined by the initial reduction of the Ni(II) complex. Therefore, large catalytic currents are observed near the Ni(II/I) redox potential, $E = E^0(\mathbf{Ni^{2+}}/\mathbf{Ni^{+}}) = -0.83$ V. Figure 12 suggests that the actual potential, E, also depends on the strength of the acid. To better quantify this influence, the half-wave potential,[63] $E_{\mathrm{p}/2}$, was plotted vs the strength of the acid for three different acid concentrations (Figure 13). Below a given $\mathrm{p}K_\mathrm{a}$ threshold, which depends on the acid concentration, $E_{\mathrm{p}/2}$ undergoes a sizable kinetic shift toward more positive values as a consequence of faster protonation rates of the reduced Ni(I) species (see eq 4). However, this shift is smaller than the positive shift of the thermodynamic potential as a result of the change in the $\mathrm{p}K_\mathrm{a}$ of the acid (see eq 2). Therefore, the stronger the acid, the higher the overpotential, as illustrated in the inset of Figure 13.

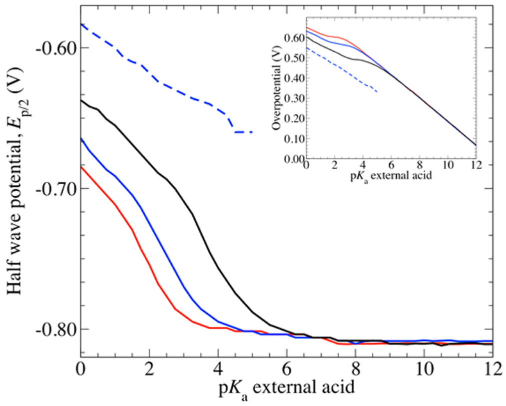

Figure 13. Half-wave potential for three different acid concentrations as a function of the strength of the acid. Red line, $[\mathrm{BH}^+] = 0.05$M; blue line, $[\mathrm{BH}^+] = 0.10$ M; black line, 0.50 M. Solid lines, ECEC process; dashed line, CECE process. In the inset, the overpotential as a function of the acid strength is also shown. All data refer to unbuffered acid solutions.

Figure 12 suggests that the lowest overpotentials are obtained for pathways involving preprotonation of Ni(II). Indeed, protonated Ni(II) species have a more positive reduction potential. For instance, the singly and doubly endo N-protonated Ni(II) species, $\mathbf{e}^{3+}$ and $\mathbf{ee}^{4+}$ (see Figures S1, S9), have a reduction potential $E^0(\mathbf{e}^{3+}/\mathbf{e}^{2+}) = -0.63$ V and $E^0(\mathbf{ee}^{4+}/\mathbf{ee}^{3+}) = -0.18$ V. Consequently, CECE or CCEE pathways operate at a considerably lower overpotential than ECEC and EECC pathways (see, for example, the dashed line in Figure 13 for the ECEC pathway). However, for $[\mathrm{Ni}(\mathrm{P}_2^{\mathrm{Ph}}\mathrm{N}_2^{\mathrm{Ph}})_2]^{2+}$, these pathways lead to very low catalytic rates (Figure 12).

Thermodynamic vs Kinetic Considerations. Thermodynamic (equilibrium) considerations provide important information about possible catalytic pathways. A thermodynamics-based analysis has been widely employed to understand the catalytic activity of homogeneous, heterogeneous, and enzymatic systems, and here, we refer to just a few recent reports.[64−66] Although it is very often used, the equilibrium approximation does not necessarily apply to chemical kinetics. To obtain accurate predictions of reaction pathways, reaction kinetics under catalytic conditions needs to be taken into account. In this paper, we have presented a comprehensive analysis of the reaction kinetics of H_2 production from acidic acetonitrile solutions catalyzed by $[\mathrm{Ni}(\mathrm{P}_2^{\mathrm{Ph}}\mathrm{N}_2^{\mathrm{Ph}})_2]^{2+}$. Here, we will compare and discuss the results presented above with a purely (standard state) thermodynamics analysis of the catalytic pathways discussed previously.[1,2]

The standard state free energy diagram of the major species involved in the H_2 production from an acetonitrile solution of $[(\mathrm{DMF})\mathrm{H}]^+$ is shown in Figure 14. Free energies are reported at an applied potential of $E = -0.995$ V, which is the potential at which the TOF is measured in a CV experiment at a scan rate of 50 mV/s. On the basis of thermodynamic considerations, one concludes that at this potential, catalysis will follow mostly EECC pathways involving both endo and exo protonation of the pendant amines (pathway indicated by bold dashed arrows in Figure 14). Consistent with the quantitative kinetic analysis discussed above, Figure 14 shows that at $E = -0.995$ V the reduced $\mathbf{Ni^0}$ intermediate represents a critical branching point in the catalytic cycle, leading to either $\mathbf{e}^+$ or $\mathbf{x}^+$.

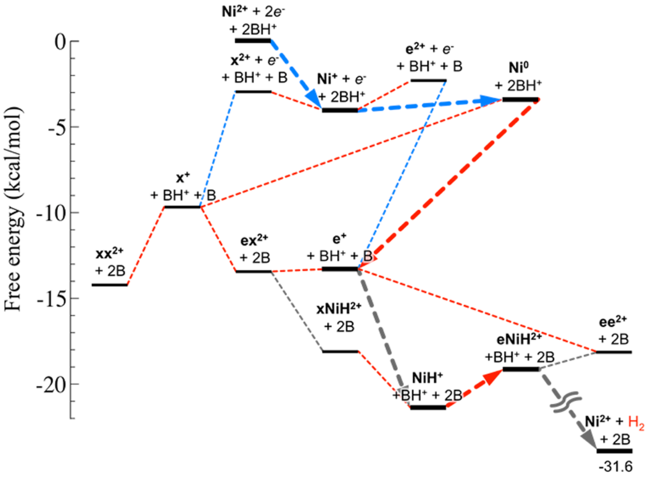

Figure 14. Standard state free energy diagram representing the main species involved in the catalytic production of H_2 from acetonitrile solutions of $[(\mathrm{DMF})\mathrm{H}]^+$ (indicated as BH^+) acetonitrile solutions according to ECEC and EECC pathways under standard conditions (catalyst, BH^+ and B at 1 M concentration under 1 atm H_2) at an electrode potential equal to −0.995 V. Reaction pathways among intermediates are indicated with dashed lines. The bold dashed lines represent the most probable path for H_2 production based on purely thermodynamic considerations. See Figure 5 for further details.

Most important, a purely thermodynamic analysis clearly suggests that exo protonation might be detrimental to catalysis.[1,2] In fact, formation of the off-cycle doubly exoprotonated Ni(0) isomer, $\mathbf{xx}^{2+}$ (see Figure 5), is expected to be a kinetic trap because this species can rejoin the main catalytic cycle only via the high-energy monoprotonated intermediate $\mathbf{x}^{+}$. The difference in energy between singly and doubly protonated Ni(0) (ΔG^0 = 7 kcal/mol in $[(\mathrm{DMF})\mathrm{H}]^+$) indicates that the rate of protonation of $\mathbf{x}^{+}$ to give $\mathbf{xx}^{2+}$ is higher than the rate of deprotonation of $\mathbf{xx}^{2+}$ to give $\mathbf{x}^{+}$. The very large excess of acid employed in typical experimental conditions (1000-fold or more; see the numerical experiment of Figure 8) further exacerbates this difference in rates.

However, from the energy diagram of Figure 14, it is not possible to quantify the detrimental role of exo protonation. Just looking at the equilibrium population of protonated Ni(0) isomers under standard state conditions (Figure 15, black bars), the $\mathbf{xx}^{2+}$ species represents a negligible fraction, with the predominant species being the catalytically competent Ni(0) hydride (NiH^+). In contrast, looking at the kinetic distribution of intermediates achieved under catalytic conditions at E = −0.995 V, one reaches a very different conclusion. As illustrated in Figure 15, the kinetic population of exo protonated species attained in the sweep potential experiment of Figure 6a is much larger than the equilibrium populations. In addition, marked differences are observed in the spatial distribution of the species from the electrode surface (Figure S7). Although at the electrode surface (Figure 15, red bars), the most populated species is still $\mathbf{NiH}^{+}$, with comparable populations of $\mathbf{xx}^{2+}$ and $\mathbf{xNiH}^{2+}$, in the diffusion layer (Figure 15, blue bars), the $\mathbf{xx}^{2+}$ isomer is by far the predominant species. It turns out that the $\mathbf{xx}^{2+}$ is the second most populated species in the diffusion layer (17%), after the nonprotonated Ni(II) complex (80%).

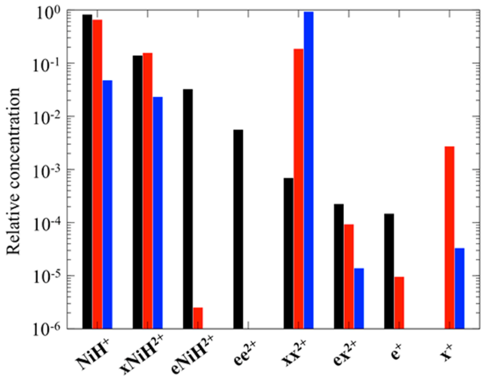

Figure 15. Relative population of protonated Ni(0) intermediates. Black bars, equilibrium population; red bars, steady state population at the surface of the electrode; blue bars, steady state population in the diffusion layer (see Supporting Information for more details). Red and blue bars refer to catalytic conditions at E = −0.995 V (see Figure 6a and Figure 8a for further details). If not present, the relative population is $<10^{-6}$.

The difference between equilibrium concentrations and (quasi) steady state concentrations suggests that standard state reaction free energies most likely do not provide a good description of the reaction profiles under catalytic conditions (e.g., cyclic voltammetry conditions). To better quantify this difference, we compared the equilibrium constants, $K_{\mathrm{eq}}^{(i)}$, and reaction quotients with steady state concentrations, $Q^{(i)}$, for each reaction, i, of the macrokinetic model of Figure 5. To facilitate this comparison, we will report $K_{\mathrm{eq}}^{(i)}$ and $Q^{(i)}$ on a free energy scale:

$$\Delta G_i^0 = -RT \ln K_{\mathrm{eq}}^{(i)}$$

and

$$\Delta G_i^* = -RT \ln Q^{(i)}$$

The difference $\Delta G_i = \Delta G_i^0 - \Delta G_i^* = \Delta G_i^0 + RT \ln Q^{(i)}$ quantifies how much steady state conditions differ from equilibrium conditions. Therefore, it provides us with an estimate of the deviation of the standard state reaction free energies ΔG_i^0 from the steady state thermodynamic driving force, ΔG_i^*. A detailed discussion on the actual calculation of ΔG_i^* is given in the Supporting Information. It is important to point out that, although the ΔG_i^0's in a cycle sum to zero (or to the overpotential in the case that H_2 is released), the sum of the ΔG_i^* values is not necessarily zero.

The difference between ΔG_i^0 and ΔG_i^* is reported in Figure 16 (red numbers). As can be seen, for most of the reactions, these two quantities agree within 1 kcal/mol. However, a few notable exceptions exist, which involve the reactions at the branching points related to the protonation of the $\mathbf{Ni}^{0}$, $\mathbf{x}^{+}$ and $\mathbf{NiH}^{+}$ species (highlighted values in Figure 16). The ΔG_i^* values for the exo protonation of these species are smaller (more negative) than the corresponding ΔG_i^0 values ($\Delta G_i > 0$), whereas the ΔG_i^* values for endo protonation are considerably greater than the ΔG_i^0 values ($\Delta G_i < 0$). This means that, under steady state conditions, the formation of the kinetically trapped doubly protonated $\mathbf{xx}^{2+}$ species biases the protonation of $\mathbf{Ni}^{0}$ and $\mathbf{x}^{+}$ toward the formation of $\mathbf{xx}^{2+}$ and disfavors the endo protonation of $\mathbf{NiH}^{+}$ to $\mathbf{eNiH}^{2+}$ by reducing the amount of $\mathbf{NiH}^{+}$, confirming the detrimental role of exo protonation. It is worth pointing out that the ΔG_i^* and ΔG_i^0 values become very similar when the exo protonation channels are shut down. Consistent with the analysis provided above, this suggests that the deviation between $\Delta G_i^*$and ΔG_i^0 is a consequence of the kinetic coupling between endo and exo protonation pathways during catalysis.

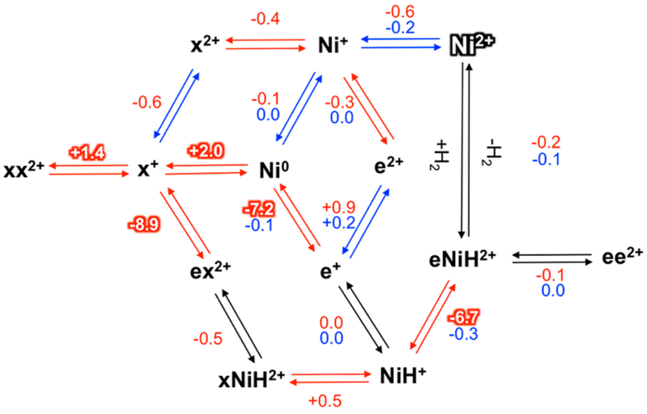

Figure 16. Difference, $\Delta G_i = \Delta G_i^0 - \Delta G_i^*$, between standard state reaction free energies (ΔG_i^0) and (nonequilibrium) steady state reaction free energies (ΔG_i^*) for the full kinetic model (red numbers) and the model with all exo protonation channels shut down (blue numbers) at a potential of E = −0.995 V. ΔG_i values larger than 1 kcal/mol are highlighted. See Figure 5 and Figure 6 for further details. Free energies are reported in kcal/mol.

In summary, the detrimental role of exo protonation can be postulated from a thermodynamic analysis, but cannot be quantified without including kinetic arguments. In addition, a thermodynamic analysis does not allow for a simple and clear prediction of the acid concentration dependence of catalysis. Overall, although thermodynamics provides fast and important initial information, it is not possible to make reliable predictions of catalytic pathways and rates from thermodynamics alone. This is clearly shown by a thermodynamic analysis of the possible catalytic pathways in strong acidic media where preprotonation of Ni(II) may become a viable catalytic pathway. As shown in Figure S10, with an external acid with a $pK_a = 1.0$, thermodynamic consideration suggest that appreciable H_2 production should proceed only via CECE routes. The kinetic analysis reported in Figure 12 tells us that this is, indeed, the favored pathway for $E = -0.995$ V and $pK_a = 1.0$, but the corresponding catalytic rate is negligible. A simple comparison of the standard state free energy diagram for H_2 production in $[(DMF)H]^+$ (Figure 14) with that in an acidic medium with $pK_a = 1.0$ (Figure S10) does not explain the large difference in catalytic rates between the two acids (at $E = -0.995$ V with [cat] = 0.43 mM and $[BH^+]$ = 0.22M, TOF = 480 and 1 s^{-1} in $[(DMF)H]^+$ and $pK_a = 1.0$, respectively).

CONCLUSIONS

Design of catalysts with improved performances requires a systematic approach to exploring ligands with specific functionalities and finely tailored electronic and steric properties to tune the energetics of reaction intermediates and the kinetic barriers between them. Thermodynamics schemes based on the knowledge of pK_a values, hydride donor abilities and redox potentials and other relevant thermodynamic properties have demonstrated themselves very effective for exploring possible reaction pathways. They also allow identifying high-energy intermediates, which may represent a catalytic bottleneck, and low-energy intermediates, which may represent a thermodynamic sink. Our group and others have employed such schemes to explore a variety of catalytic processes. However, such schemes rely on equilibrium thermodynamic assumptions, which may not necessarily apply under catalytic conditions. It is therefore important to address the general question of how reliable purely thermodynamic descriptors of reactivity are in predicting the design criteria of a catalyst. Catalysis is a kinetic phenomenon, and reactivity is performed not at equilibrium, but rather, in a kinetic steady state, in which the concentrations of species may differ markedly from their equilibrium distribution.

In this study, working on a well-established catalyst for H_2 production,[7] we performed a detailed kinetic analysis of the catalytic pathways to assess the limitations of our current (standard state) thermodynamic analysis with respect to prediction of optimal catalyst performance. To this end, we developed a microkinetic model based on accurate ab initio simulations for H_2 production from acetonitrile solutions of $[(DMF)H]^+$ catalyzed by $[Ni(P_2^{Ph}N_2^{Ph})_2]^{2+}$.[17] The model was validated against available experimental data, and it reproduces the observed turnover rate as a function of the acid concentration (Figure 8) and catalytic conditions remarkably well (applied potential, pure acid solutions vs 1:1 $[(DMF)H]^+$/DMF solutions; Figure 6). Using this kinetic model, we discerned the main factors limiting catalysis. The major detrimental contribution comes from the availability of multiple protonation sites (Figure 8), which introduce branching points along the catalytic pathway (i.e., endo versus exo protonation of the pendant amine with respect to the metal center), making less productive routes accessible or leading to off-cycle species (i.e., exo N-doubly protonated isomers Ni(0), $\mathbf{xx}^{2+}$; see Figure 2 and Figure 5), which must be deprotonated and then reprotonated to rejoin the main catalytic path. We found that intermolecular protonation and deprotonation reactions (Figure 9) are rate-limiting, being much less favorable than intramolecular proton transfers. The model allowed analysis of the effect of catalytic conditions on rate and overpotential and determination of the most probable pathway for a given condition (Figure 9 and Figure 12). Taken altogether, these results represent fundamental insights toward the design of improved catalysts.

Another important outcome of this study is that protonation/deprotonation barriers can be estimated from simple linear free energy relationships. We contend that similar relationships are applicable for other processes, such as intramolecular proton movement and H−H bond formation. This finding allows us to combine already established predictions of reaction energies based on simple thermodynamic quantities (such as pK_a values) with the kinetic model proposed here to give a powerful tool to explore catalytic performance under realistic conditions and, ultimately, to guide the design of new catalysts. The next step toward this goal is to establish correlations between activation barriers and electron-donating/-withdrawing characteristics of the substituents and the substrate (i.e., acid or base), and their steric properties. This mapping should be achievable through computed Taft-like relations[67] linking chemical composition to electronic and steric effects. This is a subject of current research in our laboratory. The procedure outlined here is very general and not limited to the class of catalysts discussed in this paper. Indeed, a thermodynamics-based exploration of the free energy landscape of possible intermediates and pathways between them for chemical and electrochemical catalytic processes is ubiquitous; the typical underlying chemical processes involve electron transfer (redox potentials), proton transfer (pK_a values), hydride transfer (hydride donor abilities), etc. Knowledge of these properties allows for a quick estimate of reaction free energies[1] and activation barriers via linear free energy relationships parametrized by ab initio calculations on selected molecules.

Finally, the kinetic analysis reported in this paper allowed us to quantify the limitations of a purely thermodynamic approach. We have shown that deviations from the thermodynamic predictions of relative free energy (population) of species arise from the kinetic coupling between reaction pathways during catalysis, resulting in the diversion in the reaction flux along the most kinetically accessible routes, as opposed to the thermodynamically favorable ones. This information is accessible only by a detailed kinetic analysis of the entire reaction network and has clear ramifications for catalyst design. This can be best understood by comparing the free energies, ΔG^*, under reaction conditions and how they differ from standard state reaction free energies, ΔG^0. We illustrate both of these quantities for the current complex $[Ni(P_2^{Ph}N_2^{Ph})_2]^{2+}$ in Figure 16 (see Supporting Information for a detailed discussion). In the majority of cases, the agreement between ΔG^* and ΔG^0 is remarkable, with deviations of only 1 kcal/mol. However, this is not uniformly true. There are also a few significant deviations on the order of 6−9 kcal/mol, most notably at rate-limiting steps in the catalytic cycle. Taken all in all, our results show that thermodynamics can provide a good first assessment of the relative free energy of intermediates. This allows one to access which molecular catalysts could be worth pursuing and in which general direction they need to be modified to enhance some aspects of the catalysis. On the other hand, one needs to be cognizant that this assessment is not truly quantitative since it does not apply to in operando conditions and that branching points in the mechanism may prohibit its use if one chooses to *maximize* the potential performance of a catalytic reaction.

■ COMPUTATIONAL METHODS

General Strategy. The computational modeling of the catalytic production of H_2 by acetonitrile solutions of protonated dimethylformamide, $[(DMF)H]^+$, requires the modeling of (intermolecular) protonation and deprotonation steps, intramolecular proton transfers, chair/boar conformational changes, and H−H bond formation. Intramolecular proton transfers and conformational changes can be easily described using quantum chemistry methodologies based on a stationary point search on the potential energy surface. In previous publications,[19,21,32,38,51,68−70] it was shown that these calculations, complemented by harmonic thermal and entropic corrections along with a continuum description of the solvent, are adequately accurate to describe intramolecular processes, especially when explicit solvent molecules engaging hydrogen bonds with the catalysts are employed.[21]

In contrast, the modeling of the acid/base reactions required for the intermolecular protonation/deprotonation steps is difficult to model within the standard quantum chemistry computational framework. The major problems encountered involve the calculation of (1) the entropic contribution to the reaction free energy and (2) the activation free energy barrier, which are not reliably accounted for using a continuum description of the solvent in large and very flexible molecules. The inclusion of a few explicit molecules of the solvent is still problematic because of the dynamical character of the acid/base encounter complex. Instead, molecular dynamics simulations represent a consolidated tool to explore at finite temperature the complex interplay between solvent, acid/base, and the Ni complex.[19,71−76] Therefore, protonation/deprotonation steps were explored via hybrid quantum mechanics/molecular dynamics (QM/MM) simulations along with enhanced sampling techniques for free energy calculations.[77] These simulations are computationally demanding and cannot be applied to the study of all of the possible intermolecular processes involved in the isomerization. Rather, they were performed on selected reactions, and the results extended to the other condition as discussed above.

QM/MM Molecular Dynamics Simulations. The binding and dissociation free energy of $[(DMF)H]^+$ and DMF to the Ni catalyst was calculated via ab initio QM/MM Born−Oppenheimer, metadynamics molecular dynamics simulations.[77−79] The Ni catalyst and $[(DMF)H]^+$ or DMF were treated at the QM level, whereas the solvent was described using an empirical potential.[80] Simulations were performed within the density functional theory (DFT) framework using the PBE exchange and correlation functional,[81] augmented with Grimme's correction for the dispersion energy (PBE + D2).[82] The van der Waals parameters for the interaction between the QM atoms and the solvent were calculated using Lennard-Jones potentials, as described elsewhere.[19] The QM/MM simulations were performed using the CP2K package[26] in the canonical ensemble[83] using an integration time step of the equation of motion of 0.2 fs.

The metadynamics technique[77,84] was employed to obtain the free energy profile for the binding and dissociation of $[(DMF)H]^+$ and DMF as well as the intermolecular proton transfer steps. Metadynamics is an adaptive biasing potential technique that disfavors configurations that have been already explored and, consequently, favors situations that would have been poorly explored thermally. The bias can be applied to any physical quantity describing the process being studied. To increase the sampling efficiency, a variant of metadynamics called multiple-walker metadynamics,[77] in which replicas of the system ("walkers") are propagated in time, all contributing to the exploration of the same free energy surface defined by a given set of collective variables. Binding of $[(DMF)H]^+$ and proton transfer between acid and catalysts were followed using as collective variables (1) the distance between the O atom of $[(DMF)H]^+$ and the Ni center, $d(\mathrm{Ni{-}O})$, and (2) the asymmetric stretching coordinate defined by the N atom of the target pendant amine, the $[(DMF)H]^+$ protic H atom, and the O atom of $[(DMF)H]^+$, $\nu = d(\mathrm{N{-}H}) - d(\mathrm{O{-}H})$ (Figure S11). The choice of these collective variables has been based on previous simulations of proton transfer processes.[33,75,85] Gaussian functions of 0.1 kcal/mol in height and with a width of 0.1 Å were employed to bias the phase space. The Gaussian function deposition time was 40 fs. Depending on the reactions studied, a number of replicas between 10 and 20 was used to sample the free energy surface. QM/MM simulations were run until each replica visited all minima, which amounted to a simulation time between 30 to 80 ps per replica, depending on the systems.

The starting configurations for the QM/MM multiple-walker metadynamics simulations were prepared as follows: (1) The Ni complex and $[(DMF)H]^+$ association complex in its gas-phase equilibrium geometry were solvated by more than 1000 acetonitrile solvent molecules in a cubic box. The solvent was equilibrated at a constant pressure (p = 1 bar)[86,87] and a constant temperature (T = 300 K) for 4 ns. (2) A constant volume, constant temperature simulation was run at the equilibrium density of the solution as obtained from the previous simulation. In these simulations, the catalyst and $[(DMF)H]^+$ (DMF) were kept frozen in their DFT optimized structure in the gas phase. Point charges calculated according to the Amber RESP procedure[88] were employed to describe the electrostatic interaction between the catalyst and solvent. (3) Configurations equally spaced in time for the last 2 ns of the MD run were chosen. Each configuration was relaxed at QM/MM and then (4) further equilibrated at 300 K by a 5 ps constant volume and constant-temperature QM/MM simulation. The randomization of the solvent around the catalyst via force field-based MD simulations is extremely important for a statistically meaningful exploration of the free energy landscape. All the classical simulations of steps 1, 2, and 3 above were performed with the GROMACS package.[89]

Quantum Chemistry Calculations. Most of the energetics relative to intramolecular processes were taken from previous publications.[19,21] Missing quantities were calculated using DFT calculations with the hybrid B3P86 exchange and correlation functional.[90−92] Activation barriers and reaction free energies are reported in Table S2. The Stuttgart basis set with effective core potential was employed for the Ni atom[93] and 6-31G* for all nonmetal atoms with additional *p* polarization functions on the protic or hydridic hydrogens.[94] Harmonic vibrational frequencies were calculated at the optimized structures using the same level of theory to estimate the zero-point energy and thermal contributions (T = 298 K and p = 1 bar) to the gas-phase free energy. We used solvation free energies calculated using a mixed cluster/continuum description of the solvent acetonitrile.[95] Specifically, all of the solvent molecules engaging hydrogen bond interactions with the catalyst, the acid or its conjugate base were explicitly included in the calculation. The initial location of these explicit solvent molecules was inferred from the MD simulations described above. The rest of the solvent was treated using a self-consistent reaction field model at the same level of theory as for the other steps. The continuum polarizable conductor model (CPCM) was used with Bondi radii.[96] Also in this case, standard state corrections to solvation energy were applied. Redox potentials and pK_a values of the N-protonated species (Table S1) were calculated using isodesmic reaction schemes and linear free energy relationships, as illustrated elsewhere.[2,3] All these calculations were performed with Gaussian09.[97]

Kinetic Modeling. The coupled kinetic equations representing the reaction network of Figure 5 and Figure S9 were solved numerically using an in-house program (available upon request) based on the SUNDIAL package for systems of stiff ordinary differential equations.[98] Two types of kinetic modeling were performed. First, we solved the microkinetic model schematically represented in Figure 5 taking into account all of the elementary steps deduced from the ab initio calculations described above and previous publications.[19,21,33,34,68] A total of 32 elementary reactions were considered (including homoconjugation of the acid). In the later stage, we solved the macrokinetic model depicted in Figure S9 by considering only the main reactions involved, e.g., $\mathbf{Ni}^{+} + [(DMF)H]^{+} \leftrightarrows \mathbf{e}^{2+} + DMF$ and $\mathbf{Ni}^{+} + [(DMF)H]^{+} \leftrightarrows \mathbf{x}^{2+} + DMF$ (Figure 4), with activation barriers obtained from the linear free energy relationship reported in eq 5, for a total of 36 reactions. Mass transfer by diffusion was included in both kinetic models according to the Fick's law. No migration of ions due to the electric potential was considered. Diffusion coefficients of the various catalytic species were calculated from the force field-based molecular dynamics simulations described above and are given in (Table S1). The diffusion coefficients of $[(DMF)H]^{+}$, DMF, and H_2 in acetonitrile were calculated, with additional simulations based on the OPLS/AA force field for $[(DMF)H]^{+}$, DMF, and $[(DMF)_2H]^{+}$,[99−101] and the force field of ref 102 for H_2 (Table S1), which to the best of our knowledge represents the best choice for these molecules. The activation for the formation of the homoconjugated pair, $(DMF)_2H^{+}$, was assumed to be equal to the fastest intramolecular proton transfer within the catalyst, i.e. $\mathbf{e}^{+} \rightarrow \mathbf{NiH}^{+}$ ($\Delta G^{\ddagger}$ = 2.8 kcal/mol). Activation barriers of thermochemical steps were converted to rate constants using the Eyring equation. Electrochemical reactions were allowed only at the surface of the electrode and were described according to the Butler−Volmer kinetics.[63] Specifically, for a given redox proces, $O + e^{-} \leftrightarrows R$ (e.g., $\mathbf{Ni}^{2+} + e^{-} \leftrightarrows \mathbf{Ni}^{+}$), the forward rate constant (i.e., one-electron reduction), $\overrightarrow{k}$, and the reverse rate constant (i.e., one-electron oxidation), $\overleftarrow{k}$, were calculated according the equations

$$\overrightarrow{k} = k_0 \exp\left[-\frac{\alpha F}{RT}(E - E_0)\right]$$

and

$$\overleftarrow{k} = k_0 \exp\left[\frac{(1 - \alpha)F}{RT}(E - E_0)\right]$$

where k_0 is the heterogeneous standard electron transfer rate constant, α is the transfer coefficient, E is the applied potential, and E_0 is the standard state redox potential. On the basis of a number of electrochemical measurements on $[Ni(P^{R}_{2}N^{R'}_{2})_2]^{2+}$ complexes carried out in our laboratory, calculations were performed using k_0 = 4 cm/s, while a customary transfer coefficient α = 1/2 was assumed. The electrode was treated as an infinite flat surface located at x = 0. The diffusion part of the kinetic equations was solved by finite difference on an exponential expanding grid,[103]

$$x_i = \Delta x e^{ai} \quad i = 0, 1, 2, \ldots$$

with Δx = 10 Å and a = 0.5, imposing semi-infinite boundary conditions. Calculated currents are referred to a surface area of the electrode of 1 cm^2. Experimental currents have been normalized to this electrode area.

ASSOCIATED CONTENT

Supporting Information

The Supporting Information is available free of charge on the ACS Publications website at DOI: 10.1021/acscatal.5b01152.

> Additional computational details and discussion, including the parameters employed in the kinenitc analysis, ab initio-derived free energy landscapes for the protonation reactions, effect of homoconjugation of the acid on the catalytic rate, and the calculation of the steady free energies (PDF)

AUTHOR INFORMATION

Corresponding Author

*E-mail: simone.raugei@pnnl.gov.

Notes

The authors declare no competing financial interest.

ACKNOWLEDGMENTS

We thank Dr. W. J. Shaw, Dr. Aaron M. Appel, and Dr. M. L. Helm for fruitful discussions. This research was supported as part of the Center for Molecular Electrocatalysis, an Energy Frontier Research Center funded by the U.S. Department of Energy, Office of Science, Office of Basic Energy Sciences. Pacific Northwest National Laboratory is operated by Battelle for the U.S. Department of Energy. Computer Resources were provided by the W. R. Wiley Environmental Molecular Sciences Laboratory (EMSL), a DOE Office of Science User Facility located at Pacific Northwest National Laboratory and sponsored by DOE's Office of Biological and Environmental Research. Computer resources were also provided by the National Energy Research Computing Center (NERSC) at the Lawrence Berkeley National Laboratory.

REFERENCES

(1) Raugei, S.; DuBois, D. L.; Rousseau, R.; Chen, S.; Ho, M.-H.; Bullock, R. M.; Dupuis, M. *Acc. Chem. Res.* **2015**, *48*, 248−255.

(2) Chen, S.; Ho, M.-H.; Bullock, R. M.; DuBois, D. L.; Dupuis, M.; Rousseau, R.; Raugei, S. *ACS Catal.* **2014**, *4*, 229−242.

(3) Chen, S.; Rousseau, R.; Raugei, S.; Dupuis, M.; DuBois, D. L.; Bullock, R. M. *Organometallics* **2011**, *30*, 6108−6118.

(4) DuBois, D. L.; Bullock, R. M. *Eur. J. Inorg. Chem.* **2011**, *2011*, 1017−1027.

(5) Wiedner, E. S.; Appel, A. M. *J. Am. Chem. Soc.* **2014**, *136*, 8661−8668.

(6) Rakowski DuBois, M.; DuBois, D. L. *Chem. Soc. Rev.* **2009**, *38*, 62−72.

(7) DuBois, D. L. *Inorg. Chem.* **2014**, *53*, 3935−3960.

(8) Deshmukh, S. R.; Mhadeshwar, A. B.; Vlachos, D. G. *Ind. Eng. Chem. Res.* **2004**, *43*, 2986−2999.

(9) Mhadeshwar, A. B.; Wang, H.; Vlachos, D. G. *J. Phys. Chem. B* **2003**, *107*, 12721−12733.

(10) Mhadeshwar, A. B.; Vlachos, D. G. *Catal. Today* **2005**, *105*, 162−172.

(11) Dossin, T.; Reyniers, M.; Marin, G. *Appl. Catal., B* **2006**, *62*, 35−45.

(12) Greeley, J.; Jaramillo, T. F.; Bonde, J.; Chorkendorff, I.; Nørskov, J. K. *Nat. Mater.* **2006**, *5*, 909−913.

(13) Nørskov, J. K.; Bligaard, T.; Rossmeisl, J.; Christensen, C. H. *Nat. Chem.* **2009**, *1*, 37−46.

(14) Marin, G.; Yablonsky, G. S. *Kinetics of Chemical Reactions*; Wiley VCH: Weinheim, 2011.

(15) Ruscic, B. *Int. J. Quantum Chem.* **2014**, *114*, 1097−1101.

(16) Peterson, K. A.; Feller, D.; Dixon, D. A. *Theor. Chem. Acc.* **2012**, *131*, 1070.

(17) Kilgore, U. J.; Roberts, J. A. S.; Pool, D. H.; Appel, A. M.; Stewart, M. P.; DuBois, M. R.; Dougherty, W. G.; Kassel, W. S.; Bullock, R. M.; DuBois, D. L. *J. Am. Chem. Soc.* **2011**, *133*, 5861−5872.

(18) Kilgore, U. J.; Stewart, M. P.; Helm, M. L.; Dougherty, W. G.; Kassel, W. S.; DuBois, M. R.; DuBois, D. L.; Bullock, R. M. *Inorg. Chem.* **2011**, *50*, 10908−10918.

(19) Raugei, S.; Chen, S.; Ho, M.-H.; Ginovska-Pangovska, B.; Rousseau, R. J.; Dupuis, M.; DuBois, D. L.; Bullock, R. M. *Chem. - Eur. J.* **2012**, *18*, 6493−6506.

(20) Pool, D. H.; Stewart, M. P.; O'Hagan, M.; Shaw, W. J.; Roberts, J. A. S.; Bullock, R. M.; DuBois, D. L. *Proc. Natl. Acad. Sci. U. S. A.* **2012**, *109*, 15634−15639.

(21) Ho, M.-H.; Raugei, S.; Rousseau, R.; Dupuis, M.; Bullock, R. M. *J. Chem. Theory Comput.* **2013**, *9*, 3505−3514.

(22) Roberts, J. A. S.; Bullock, R. M. *Inorg. Chem.* **2013**, *52*, 3823−3835.

(23) Bullock, R. M. *Catalysis without Precious Metals*; Wiley-VCH: Weinheim, 2010.

(24) Wang, M.; Chen, L.; Sun, L. *Energy Environ. Sci.* **2012**, *5*, 6763−6778.

(25) Du, P.; Eisenberg, R. *Energy Environ. Sci.* **2012**, *5*, 6012−6021.

(26) Thoi, V. S.; Sun, Y.; Long, J. R.; Chang, C. J. *Chem. Soc. Rev.* **2013**, *42*, 2388−2400.

(27) McKone, J. R.; Marinescu, S. C.; Brunschwig, B. S.; Winkler, J. R.; Gray, H. B. *Chem. Sci.* **2014**, *5*, 865−878.

(28) Cook, T. R.; Dogutan, D. K.; Reece, S. Y.; Surendranath, Y.; Teets, T. S.; Nocera, D. G. *Chem. Rev.* **2010**, *110*, 6474−6502.

(29) Nocera, D. G. *Acc. Chem. Res.* **2012**, *45*, 767−776.

(30) Ginovska-Pangovska, B.; Dutta, A.; Reback, M. L.; Linehan, J. C.; Shaw, W. J. *Acc. Chem. Res.* **2014**, *47*, 2621−2630.

(31) Bullock, R. M.; Appel, A. M.; Helm, M. L. *Chem. Commun.* **2014**, *50*, 3125−3143.

(32) Das, P.; Ho, M.-H.; O'Hagan, M.; Shaw, W. J.; Morris Bullock, R.; Raugei, S.; Helm, M. L. *Dalton Trans.* **2014**, *43*, 2744−2754.

(33) O'Hagan, M.; Ho, M.-H.; Yang, J. Y.; Appel, A. M.; DuBois, M. R.; Raugei, S.; Shaw, W. J.; DuBois, D. L.; Bullock, R. M. *J. Am. Chem. Soc.* **2012**, *134*, 19409−19424.

(34) O'Hagan, M.; Shaw, W. J.; Raugei, S.; Chen, S.; Yang, J. Y.; Kilgore, U. J.; DuBois, D. L.; Bullock, R. M. *J. Am. Chem. Soc.* **2011**, *133*, 14301−14312.

(35) Fontecilla-Camps, J. C.; Volbeda, A.; Cavazza, C.; Nicolet, Y. *Chem. Rev.* **2007**, *107*, 4273−4303.

(36) Vincent, K. A.; Parkin, A.; Armstrong, F. A. *Chem. Rev.* **2007**, *107*, 4366−4413.

(37) Helm, M. L.; Stewart, M. P.; Bullock, R. M.; DuBois, M. R.; DuBois, D. L. *Science* **2011**, *333*, 863−866.

(38) Stewart, M. P.; Ho, M.-H.; Wiese, S.; Lindstrom, M. L.; Thogerson, C. E.; Raugei, S.; Bullock, R. M.; Helm, M. L. *J. Am. Chem. Soc.* **2013**, *135*, 6033−6046.

(39) Darmon, J. M.; Raugei, S.; Liu, T.; Hulley, E. B.; Weiss, C. J.; Bullock, R. M.; Helm, M. L. *ACS Catal.* **2014**, *4*, 1246−1260.

(40) Liu, T.; DuBois, D. L.; Bullock, R. M. *Nat. Chem.* **2013**, *5*, 228−233.

(41) Fang, M.; Wiedner, E. S.; Dougherty, W. G.; Kassel, W. S.; Liu, T.; DuBois, D. L.; Bullock, R. M. *Organometallics* **2014**, *33*, 5820−5833.

(42) Hulley, E. B.; Welch, K. D.; Appel, A. M.; DuBois, D. L.; Bullock, R. M. *J. Am. Chem. Soc.* **2013**, *135*, 11736−11739.

(43) Wiedner, E. S.; Appel, A. M.; DuBois, D. L.; Bullock, R. M. *Inorg. Chem.* **2013**, *52*, 14391−14403.

(44) Abou Hamdan, A.; Dementin, S.; Liebgott, P.-P.; Gutierrez-Sanz, O.; Richaud, P.; De Lacey, A. L.; Rousset, M.; Bertrand, P.; Cournac, L.; Léger, C. *J. Am. Chem. Soc.* **2012**, *134*, 8368−8371.

(45) McIntosh, C. L.; Germer, F.; Schulz, R.; Appel, J.; Jones, A. K. *J. Am. Chem. Soc.* **2011**, *133*, 11308−11319.

(46) Hou, J.; Fang, M.; Cardenas, A. J. P.; Shaw, W. J.; Helm, M. L.; Bullock, R. M.; Roberts, J. A. S.; O'Hagan, M. *Energy Environ. Sci.* **2014**, *7*, 4013−4017.

(47) Dutta, A.; Roberts, J. A. S.; Shaw, W. J. *Angew. Chem., Int. Ed.* **2014**, *53*, 6487−6491.

(48) Darmon, J. M.; Kumar, N.; Hulley, E. B.; Weiss, C. J.; Raugei, S.; Bullock, R. M.; Helm, M. L. *Chem. Sci.* **2015**, *6*, 2737−2745.

(49) Dutta, A.; DuBois, D. L.; Roberts, J. A. S.; Shaw, W. J. *Proc. Natl. Acad. Sci. U. S. A.* **2014**, *111*, 16286−16291.

(50) Ho, M.-H.; Chen, S.; Rousseau, R.; Dupuis, M.; Bullock, R. M.; Raugei, S. Bio-Inspired Molecular Catalysts for Hydrogen Oxidation and Hydrogen Production. In *Applications of Molecular Modeling to Challenges in Clean Energy*; Fitzgerald, G., Govind, N., Eds.; American Chemical Society: Washington, DC, 2013; Vol. *1133*, pp 89−111.

(51) Yang, J. Y.; Chen, S.; Dougherty, W. G.; Kassel, W. S.; Bullock, R. M.; DuBois, D. L.; Raugei, S.; Rousseau, R.; Dupuis, M.; DuBois, M. R. *Chem. Commun.* **2010**, *46*, 8618−8620.

(52) Yang, J. Y.; Smith, S. E.; Liu, T.; Dougherty, W. G.; Hoffert, W. A.; Kassel, W. S.; DuBois, M. R.; DuBois, D. L.; Bullock, R. M. *J. Am. Chem. Soc.* **2013**, *135*, 9700−9712.

(53) Wilson, A. D.; Shoemaker, R. K.; Miedaner, A.; Muckerman, J. T.; DuBois, D. L.; DuBois, M. R. *Proc. Natl. Acad. Sci. U. S. A.* **2007**, *104*, 6951−6956.

(54) Appel, A. M.; Helm, M. L. *ACS Catal.* **2014**, *4*, 630−633.

(55) Felton, G. A. N.; Glass, R. S.; Lichtenberger, D. L.; Evans, D. H. *Inorg. Chem.* **2006**, *45*, 9181−9184.

(56) Nicholson, R. S.; Shain, I. *Anal. Chem.* **1964**, *36*, 706−723.

(57) Saveant, J. M.; Vianello, E. *Electrochim. Acta* **1965**, *10*, 905−920.

(58) Savéant, J. M.; Vianello, E. *Electrochim. Acta* **1967**, *12*, 629−646.

(59) Deshmukh, S.; Vlachos, D. *Combust. Flame* **2007**, *149*, 366−383.

(60) Salciccioli, M.; Stamatakis, M.; Caratzoulas, S.; Vlachos, D. G. *Chem. Eng. Sci.* **2011**, *66*, 4319−4355.

(61) Bell, R. P. *Proc. R. Soc. London, Ser. A* **1936**, *154*, 414−429.

(62) Evans, M. G.; Polanyi, M. *J. Chem. Soc. Faraday Trans* **1936**, *32*, 1340.

(63) Bard, A. J.; Faulkner, L. R. *Electrochemical Methods: Fundamentals and Applications*; 2nd ed.; Wiley: New York, 2000.

(64) Calle-Vallejo, F.; Díaz-Morales, O. A.; Kolb, M. J.; Koper, M. T. M. *ACS Catal.* **2015**, *5*, 869−873.

(65) Blomberg, M. R. A.; Borowski, T.; Himo, F.; Liao, R.-Z.; Siegbahn, P. E. M. *Chem. Rev.* **2014**, *114*, 3601−3658.

(66) Varley, J. B.; Nørskov, J. K. *ChemCatChem* **2013**, *5*, 732−736.

(67) Taft, R. W., Jr *J. Am. Chem. Soc.* **1952**, *74*, 2729−2732.

(68) Chen, S.; Raugei, S.; Rousseau, R.; Dupuis, M.; Bullock, R. M. *J. Phys. Chem. A* **2010**, *114*, 12716−12724.

(69) Dupuis, M.; Chen, S.; Raugei, S.; DuBois, D. L.; Bullock, R. M. *J. Phys. Chem. A* **2011**, *115*, 4861−4865.

(70) Senthilnathan, D.; Giunta, P.; Vetere, V.; Kachmar, A.; Maldivi, P.; Franco, A. A. *RSC Adv.* **2014**, *4*, 5177−5187.

(71) Ivanov, I.; Chen, B.; Raugei, S.; Klein, M. L. *J. Phys. Chem. B* **2006**, *110*, 6365−6371.

(72) Cascella, M.; Raugei, S.; Carloni, P. *J. Phys. Chem. B* **2004**, *108*, 369−375.

(73) Cheng, J.; Liu, X.; VandeVondele, J.; Sulpizi, M.; Sprik, M. *Acc. Chem. Res.* **2014**, *47*, 3522−3529.

(74) Bhargava, B. L.; Yasaka, Y.; Klein, M. L. *J. Phys. Chem. B* **2011**, *115*, 14136−14140.

(75) Hassanali, A.; Giberti, F.; Cuny, J.; Kühne, T. D.; Parrinello, M. *Proc. Natl. Acad. Sci. U. S. A.* **2013**, *110*, 13723−13728.

(76) Hassanali, A. A.; Cuny, J.; Verdolino, V.; Parrinello, M. *Philos. Trans. R. Soc., A* **2014**, *372*, 20120482−20120482.

(77) Laio, A.; Gervasio, F. L. *Rep. Prog. Phys.* **2008**, *71*, 126601.

(78) Laino, T.; Mohamed, F.; Laio, A.; Parrinello, M. *J. Chem. Theory Comput.* **2005**, *1*, 1176−1184.

(79) Laino, T.; Mohamed, F.; Laio, A.; Parrinello, M. *J. Chem. Theory Comput.* **2006**, *2*, 1370−1378.

(80) Nikitin, A. M.; Lyubartsev, A. P. *J. Comput. Chem.* **2007**, *28*, 2020−2026.

(81) Perdew, J. P.; Burke, K.; Ernzerhof, M. *Phys. Rev. Lett.* **1996**, *77*, 3865−3868.

(82) Grimme, S. *J. Comput. Chem.* **2004**, *25*, 1463−1473.

(83) Martyna, G. J.; Klein, M. L.; Tuckerman, M. *J. Chem. Phys.* **1992**, *97*, 2635−2643.

(84) Laio, A.; Parrinello, M. *Proc. Natl. Acad. Sci. U. S. A.* **2002**, *99*, 12562−12566.

(85) Raugei, S.; Klein, M. L. *ChemPhysChem* **2004**, *5*, 1569−1576.

(86) Parrinello, M.; Rahman, A. *Phys. Rev. Lett.* **1980**, *45*, 1196−1199.

(87) Parrinello, M.; Rahman, A. *J. Appl. Phys.* **1981**, *52*, 7182−7190.

(88) Bayly, C. I.; Cieplak, P.; Cornell, W.; Kollman, P. A. *J. Phys. Chem.* **1993**, *97*, 10269−10280.

(89) Pronk, S.; Pall, S.; Schulz, R.; Larsson, P.; Bjelkmar, P.; Apostolov, R.; Shirts, M. R.; Smith, J. C.; Kasson, P. M.; van der Spoel, D.; Hess, B.; Lindahl, E. *Bioinformatics* **2013**, *29*, 845−854.

(90) Perdew, J. P. *Phys. Rev. B: Condens. Matter Mater. Phys.* **1986**, *34*, 7406−7406.

(91) Perdew, J. P. *Phys. Rev. B: Condens. Matter Mater. Phys.* **1986**, *33*, 8822−8824.

(92) Becke, A. D. *Phys. Rev. A: At., Mol., Opt. Phys.* **1988**, *38*, 3098−3100.

(93) Andrae, D.; Häußermann, U.; Dolg, M.; Stoll, H.; Preuß, H. *Theor. Chim. Acta* **1990**, *77*, 123−141.

(94) Rassolov, V. A.; Pople, J. A.; Ratner, M. A.; Windus, T. L. *J. Chem. Phys.* **1998**, *109*, 1223.

(95) Bryantsev, V. S.; Diallo, M. S.; Goddard, W. A., III *J. Phys. Chem. B* **2008**, *112*, 9709−9719.

(96) Bondi, A. *J. Phys. Chem.* **1964**, *68*, 441−451.

(97) Frisch, M. J.; Trucks, G. W.; Schlegel, H. B.; Scuseria, G. E.; Robb, M. A.; Cheeseman, J. R.; Scalmani, G.; Barone, V.; Mennucci, B.; Petersson, G. A.; et al. *Gaussian 09, Revision A.1*; Gaussian, Inc.: Wallingford, CT, 2009.

(98) Hindmarsh, A. C.; Brown, P. N.; Grant, K. E.; Lee, S. L.; Serban, R.; Shumaker, D. E.; Woodward, C. S. *ACM Trans. Math. Softw. TOMS* **2005**, *31*, 363−396.

(99) Jorgensen, W. L.; Maxwell, D. S.; Tirado-Rives, J. *J. Am. Chem. Soc.* **1996**, *118*, 11225−11236.

(100) Rizzo, R. C.; Jorgensen, W. L. *J. Am. Chem. Soc.* **1999**, *121*, 4827−4836.

(101) Jorgensen, W. L.; Tirado-Rives, J. *J. Am. Chem. Soc.* **1988**, *110*, 1657−1666.

(102) Alavi, S.; Ripmeester, J. A.; Klug, D. D. *J. Chem. Phys.* **2005**, *123*, 024507.

(103) Sundqvist, H.; Veronis, G. *Tellus* **1970**, *22*, 26−31.